



ALMA Observations of CO Emission from Luminous Lyman-break Galaxies at $z = 6.0293\text{--}6.2037$

Yoshiaki Ono¹ , Seiji Fujimoto^{2,3} , Yuichi Harikane^{1,4} , Masami Ouchi^{1,5,6} , Livia Vallini⁷ , Andrea Ferrara⁷ , Takatoshi Shibuya⁸ , Andrea Pallottini⁷ , Akio K. Inoue^{9,10} , Masatoshi Imanishi^{5,11} , Kazuhiro Shimasaku^{12,13} , Takuya Hashimoto¹⁴ , Chien-Hsiu Lee¹⁵ , Yuma Sugahara^{5,10} , Yoichi Tamura¹⁶ , Kotaro Kohno^{13,17} , and Malte Schramm¹⁸

¹ Institute for Cosmic Ray Research, The University of Tokyo, 5-1-5 Kashiwanoha, Kashiwa, Chiba 277-8582, Japan

² Cosmic Dawn Center (DAWN), Jagtvej 128, DK-2200 Copenhagen N, Denmark

³ Niels Bohr Institute, University of Copenhagen, Lyngbyvej 2, DK-2100 Copenhagen Ø, Denmark

⁴ Department of Physics and Astronomy, University College London, Gower Street, London WC1E 6BT, UK

⁵ National Astronomical Observatory of Japan, 2-21-1 Osawa, Mitaka, Tokyo 181-8588, Japan

⁶ Kavli Institute for the Physics and Mathematics of the Universe (WPI), The University of Tokyo, 5-1-5 Kashiwanoha, Kashiwa-shi, Chiba, 277-8583, Japan

⁷ Scuola Normale Superiore, Piazza dei Cavalieri 7, I-56126 Pisa, Italy

⁸ Kitami Institute of Technology, 165 Koen-cho, Kitami, Hokkaido 090-8507, Japan

⁹ Department of Physics, School of Advanced Science and Engineering, Faculty of Science and Engineering, Waseda University, 3-4-1, Okubo, Shinjuku, Tokyo 169-8555, Japan

¹⁰ Waseda Research Institute for Science and Engineering, Faculty of Science and Engineering, Waseda University, 3-4-1, Okubo, Shinjuku, Tokyo 169-8555, Japan

¹¹ Department of Astronomical Science, The Graduate University for Advanced Studies, SOKENDAI, Mitaka, Tokyo 181-8588, Japan

¹² Department of Astronomy, Graduate School of Science, The University of Tokyo, 7-3-1 Hongo, Bunkyo-ku, Tokyo 113-0033, Japan

¹³ Research Center for the Early Universe, Graduate School of Science, The University of Tokyo, 7-3-1 Hongo, Bunkyo-ku, Tokyo 113-0033, Japan

¹⁴ Tomonaga Center for the History of the Universe (TCHoU), Faculty of Pure and Applied Sciences, University of Tsukuba, Tsukuba, Ibaraki 305-8571, Japan

¹⁵ NSF's National Optical-Infrared Astronomy Research Laboratory, Tucson, AZ 85719, USA

¹⁶ Division of Particle and Astrophysical Science, Graduate School of Science, Nagoya University, Nagoya 464-8602, Japan

¹⁷ Institute of Astronomy, Graduate School of Science, The University of Tokyo, 2-21-1 Osawa, Mitaka, Tokyo 181-0015, Japan

¹⁸ Graduate School of Science and Engineering, Saitama University, 255 Shimo-Okubo, Sakura-ku, Saitama City, Saitama 338-8570, Japan

Received 2021 November 12; revised 2022 October 11; accepted 2022 October 28; published 2022 December 13

Abstract

We present our new Atacama Large Millimeter/submillimeter Array (ALMA) observations targeting CO(6–5) emission from three luminous Lyman-break galaxies (LBGs) at $z_{\text{spec}} = 6.0293\text{--}6.2037$ found in the Subaru/Hyper Suprime-Cam survey, whose [O III] 88 μm and [C II] 158 μm emissions have been detected with ALMA. We find a marginal detection of the CO(6–5) line from one of our LBGs, J0235–0532, at the $\simeq 4\sigma$ significance level and obtain upper limits for the other two LBGs, J1211–0118 and J0217–0208. Our $z = 6$ luminous LBGs are consistent with the previously found correlation between the CO luminosity and the infrared luminosity. The unique ensemble of the multiple far-infrared emission lines and underlying continuum fed to a photodissociation region model reveals that J0235–0532 has a relatively high density of hydrogen nuclei n_{H} that is comparable to those of low- z (U)LIRGs, quasars, and Galactic star-forming regions with high n_{H} values, while the other two LBGs have lower n_{H} consistent with local star-forming galaxies. By carefully taking account of various uncertainties, we obtain constraints on total gas mass and gas surface density from their CO luminosity measurements. We find that J0235–0532 is located below the Kennicutt–Schmidt (KS) relation, comparable to the $z = 5.7$ LBG, HZ10, previously detected with CO(2–1). Combined with previous results for dusty starbursts at similar redshifts, the KS relation at $z = 5\text{--}6$ is on average consistent with the local one.

Unified Astronomy Thesaurus concepts: Millimeter astronomy (1061); Submillimeter astronomy (1647); High-redshift galaxies (734); Galactic and extragalactic astronomy (563); Galaxy formation (595); Galaxy evolution (594); Photodissociation regions (1223); Interstellar medium (847); Molecular gas (1073); Interstellar line emission (844); CO line emission (262); Lyman-break galaxies (979)

1. Introduction

Constraining the properties of molecular gas in galaxies across cosmic time is important for understanding galaxy formation and evolution (see the reviews of Carilli & Walter 2013; Tacconi et al. 2020). Although star formation proceeds through the conversion of molecular hydrogen, H_2 , into stars, it is difficult to directly detect emission from H_2 in molecular clouds due to the lack of a permanent dipole moment

and the high temperatures necessary to excite even the lowest transitions.¹⁹ Instead, emission lines from rotational transitions of carbon monoxide, CO, are often employed to trace cold molecular gas in galaxies that is responsible for star formation activities.

Searches for CO line emission at $z \gtrsim 3$ have mainly focused on the most luminous sources such as quasars (e.g., Bertoldi et al. 2003; Walter et al. 2003; Maiolino et al. 2007; Weiß et al. 2007; Wang et al. 2013) and dusty starburst galaxies (e.g., Neri

Original content from this work may be used under the terms of the [Creative Commons Attribution 4.0 licence](https://creativecommons.org/licenses/by/4.0/). Any further distribution of this work must maintain attribution to the author(s) and the title of the work, journal citation and DOI.

¹⁹ Specifically, the two lowest H_2 rotational transitions have upper level energies of $h\nu/k_{\text{B}} = 510$ and 1015 K above ground (Dabrowski 1984), and the lowest H_2 vibrational transition is even more difficult to excite, corresponding to $h\nu/k_{\text{B}} = 6471$ K (Bolatto et al. 2013).

et al. 2003; Greve et al. 2005; Bothwell et al. 2013; Riechers et al. 2013; Weiß et al. 2013; Aravena et al. 2016; Zavala et al. 2018). For example, Riechers et al. (2010) have detected CO(2–1), CO(5–4), and CO(6–5) emission in a $z = 5.3$ dusty star-forming galaxy (SFG), AzTEC-3, and revealed a large molecular gas reservoir, maintaining its intense starburst with $\gtrsim 1000 M_{\odot} \text{ yr}^{-1}$. Another high- z example is a dusty SFG at $z = 5.7$, CRLE, whose CO(2–1) as well as [C II] 158 μm and [N II] 205 μm emissions have been detected in Pavesi et al. (2018), showing a large molecular gas reservoir with an intense starburst of $\simeq 1500 M_{\odot} \text{ yr}^{-1}$.

In contrast, little progress has been made for high- z normal SFGs such as Lyman-break galaxies (LBGs), which are more representative of the high- z galaxy population. Although a handful of CO detections have been reported in mostly lensed LBGs at $z \sim 3$ (e.g., Baker et al. 2004; Ginolfi et al. 2017), to date only a few CO detections from normal SFGs at $z > 3$ have been reported: i.e., luminous LBGs, LBG-1²⁰ and HZ10,²¹ at $z = 5.3\text{--}5.7$ (Pavesi et al. 2019; see also Riechers et al. 2014) and a likely damped Ly α absorber host, Serenity-18, at $z = 5.9$ (D’Odorico et al. 2018). CO lines from normal SFGs at $z > 3$ are typically too faint to allow for an investigation of the galaxy properties related to molecular gas components at high redshifts (e.g., Hashimoto et al. 2022), such as the gas surface density, the gas mass fraction, and the gas depletion time, and comparison with the Kennicutt–Schmidt (KS) relation (Schmidt 1959; Kennicutt 1998a), which are critically important for understanding the star formation process (e.g., Schinnerer et al. 2016; Kennicutt & De Los Reyes 2021) but have not yet been constrained well compared to those at lower redshifts.

In this study, we present our ALMA observations targeting CO(6–5) emission at $\nu_{\text{CO}(6-5)}^{\text{(rest)}} = 691.47 \text{ GHz}$ in the rest frame, corresponding to the rest-frame wavelength of $\lambda_{\text{CO}(6-5)}^{\text{(rest)}} = 433.6 \mu\text{m}$, as well as dust continuum emission in three LBGs at $z = 6$ that have been identified in the Subaru/Hyper Suprime-Cam (HSC) survey (Aihara et al. 2018). Previous optical spectroscopic observations have detected Ly α emission from the three LBGs (Matsuoka et al. 2018), and subsequent ALMA observations have detected [O III] 88 μm and [C II] 158 μm emission lines in these galaxies (Harikane et al. 2020b).

This paper is outlined as follows. After introducing our three $z = 6$ luminous LBGs in Section 2, we describe our new ALMA observations and data reduction processes in Section 3. Our results for the CO emission and dust continuum emission from the three $z = 6$ luminous LBGs are presented in Section 4. We discuss their gaseous properties in Section 5 and present a summary in Section 6. Throughout this paper, we use magnitudes in the AB system (Oke & Gunn 1983) and assume a flat universe with $\Omega_{\text{m}} = 0.3$, $\Omega_{\Lambda} = 0.7$, and $H_0 = 70 \text{ km s}^{-1} \text{ Mpc}^{-1}$. In this cosmological model, an angular dimension of 1'' corresponds to a physical dimension of 5.710 kpc at $z = 6.0$ (e.g., Equation (18) of Hogg 1999). We adopt the Chabrier (2003) initial mass function (IMF) with lower and upper mass cutoffs of $0.1 M_{\odot}$ and $100 M_{\odot}$, respectively. Where necessary to convert star formation rates (SFRs) in the literature from the Salpeter (1955) IMF and the Kroupa (2001) IMF to the Chabrier IMF, we multiply by constant factors of

²⁰ LBG-1 is also named HZ6 (Capak et al. 2015).

²¹ CRLE is serendipitously discovered in Atacama Large Millimeter/submillimeter Array (ALMA) observations targeting HZ10 (Pavesi et al. 2018).

Table 1
Summary of the Properties of Our Targets

	J1211–0118	J0235–0532	J0217–0208
R.A.	12:11:37.112	02:35:42.412	02:17:21.603
Decl.	−01:18:16.500	−05:32:41.623	−02:08:52.778
M_{UV} (mag)	−22.8	−22.8	−23.3
L_{UV} ($10^{11} L_{\odot}$)	2.7	2.9	4.3
SFR_{UV} ($M_{\odot} \text{ yr}^{-1}$)	48 ± 3	48 ± 4	76 ± 4
r_{e} (kpc) ^a	1.20	0.97 ^b	0.57
$\text{EW}_0^{\text{Ly}\alpha}$ (Å)	6.9 ± 0.8	41 ± 2	15 ± 1
β_{UV}	-2.0 ± 0.5	-2.6 ± 0.6	-0.1 ± 0.5
z_{sys}	6.0293 ± 0.0002	6.0901 ± 0.0006	6.2037 ± 0.0005
$L_{[\text{O III}]} / L_{[\text{C II}]}$	3.4 ± 0.6	8.9 ± 1.7	6.0 ± 1.7

Notes. Most of the values presented in this table have been obtained in previous studies (Matsuoka et al. 2018; Harikane et al. 2020b).

^a Half-light radius measured with the Subaru/HSC z -band images, which trace the rest UV continuum emission (Section 5.3).

^b This r_{e} value is measured with SExtractor, while the r_{e} values for the other targets are measured with GALFIT. This is because a numerical convergence problem may have occurred in the profile fitting with GALFIT for J0235–0532 (Section 5.3).

$\alpha_{\text{SC}} = 0.63$ and $\alpha_{\text{KC}} = 0.94 (= 0.63/0.67)$, respectively (Madau & Dickinson 2014).

2. Targets

To constrain the properties of molecular gas in $z = 6$ normal SFGs, we target three luminous LBGs at $z_{\text{spec}} = 6.029\text{--}6.204$: J1211–0118, J0235–0532, and J0217–0208. Their basic properties reported in previous work are summarized in Table 1. These LBGs have been spectroscopically identified with Ly α emission (Matsuoka et al. 2018) and their [O III] 88 μm , [C II] 158 μm , and dust continuum emission have been observed with ALMA (Harikane et al. 2020b). Their total SFRs, SFR_{tot} , have been estimated to be $\sim 100 M_{\odot} \text{ yr}^{-1}$ as the sum of the dust-unobscured and dust-obscured SFRs based on the rest-frame ultraviolet (UV) and infrared (IR) continuum emission, SFR_{UV} and SFR_{IR} , respectively. These SFRs are estimated by using Equations (1) and (4) of Kennicutt (1998b) and considering the conversion factor from the Salpeter IMF to the Chabrier IMF. For details, see Appendix A. Because of their moderately high total SFRs, the CO emission line fluxes of our targets are expected to be high, if their molecular gas is not already depleted by recent star formation.

Although their UV absolute magnitudes are $M_{\text{UV}} \simeq -23.0$ mag, around which the luminosity functions of galaxies and active galactic nuclei (AGNs) are almost comparable (e.g., Ono et al. 2018), their rest UV spectra exhibit no clear signatures of AGNs such as broad Ly α or N V 1240 Å, suggesting that they are normal SFGs. Note that, because they are not located in a foreground galaxy cluster field or close to a foreground massive red galaxy, they are unlikely to be affected by strong lensing. Thus, they are great laboratories in which to investigate typical properties of high- z normal SFGs with no systematic uncertainties of lensing models.

3. ALMA Observations and Data Reduction

Our targets were observed during ALMA Cycle 7 with Band 3 between 2019 October 1 and 2019 November 12 (Project code: 2019.1.00156.S; PI: Y. Ono). The number of antennas

Table 2
Summary of Our ALMA Observations and Data

Target	Date (YYYY-MM-DD)	Configuration	Central Frequencies of SPWs (GHz)	t_{int} (minutes)	PWV (mm)	σ_{cont} ($\mu\text{Jy beam}^{-1}$)	Beam FWHM	PA (deg)
(1)	(2)	(3)	(4)	(5)	(6)	(7)	(8)	(9)
J1211–0118	2019-10-01	C43-4	97.801, 99.488, 109.625, 111.500	59.5	3.4	17.4	$2''.36 \times 2''.15$	59.56
J0235–0532	2019-11-12	C43-3	96.964, 98.652, 108.825, 110.700	91.7	5.5	9.7	$3''.17 \times 2''.72$	–72.15
J0217–0208	2019-11-12	C43-3	95.434, 97.122, 107.325, 109.200	72.6	5.2	7.4	$3''.18 \times 2''.77$	70.38

Note. (1) Target ID. (2) Observation date. (3) Antenna configuration. (4) Central frequencies of the four SPWs. (5) On-source integration time. (6) Precipitable water vapor. (7) The 1σ level of the continuum image. (8) The synthesized beam FWHM in units of arcsec \times arcsec. (9) The position angle of the synthesized beam.

used in the observations is 45. The antenna configurations were C43-3 for J0235–0532 and J0217–0208, and C43-4 for J1211–0118. The maximum baselines of C43-3 and C43-4 are 500.2 m and 2617.4 m, respectively. The minimum baseline of these configurations is 15.1 m. We used four spectral windows (SPWs) with 1.875 GHz bandwidths in the frequency division mode, yielding the total frequency coverage of 7.5 GHz. The velocity resolution was set to 3.9 MHz, which corresponds to about 10 km s^{-1} . One of the SPWs was used for the CO(6–5) line and the others were used for the dust continuum. Note that CO(6–5) is the lowest CO excitation that can be observed for $z = 6$ galaxies with ALMA Bands 3–10. The details of the observations are presented in Table 2.

We reduce the ALMA data by using the Common Astronomy Software Applications (CASA; McMullin et al. 2007) package²² version 5.6.1. Using the CLEAN task, we produce continuum images and data cubes for our targets with the natural weighting. We apply a Gaussian taper with $\text{FWHM} = 2''.0$ to improve the signal-to-noise ratio (S/N) for potentially existing low-surface-brightness emission. We adopt a pixel scale of $0''.1$ and a common spectral channel bin of about 60 km s^{-1} . Table 2 presents the 1σ flux density levels and the spatial resolutions, and the synthesized beam position angles for the continuum images. Note that, although two of our targets were also observed with Northern Extended Millimeter Array (NOEMA), both show no detection, which is consistent with the ALMA results (Appendix B).

4. Results

4.1. CO(6–5)

For J0235–0532, the CO(6–5) emission line is marginally detected at the expected frequency from the systemic redshift, while for the other two targets, the CO(6–5) emission is not significantly detected. Figure 1 shows the ALMA spectra of our $z = 6$ luminous LBGs around their CO(6–5) emission line as expected from their systemic redshift measured by Harikane et al. (2020b) with the far-infrared (FIR) emission lines of [O III] and [C II]. The spectrum of J0235–0532 is extracted by placing a single beam aperture around the peak position of the CO emission in the CO(6–5) moment-zero map (velocity-integrated map; Figure 2), because the CO emission is not spatially resolved in the ALMA data. We fit Gaussian functions to the observed spectrum of J0235–0532 from 97.3 to 97.8 GHz and obtain the best-fit Gaussian function as presented in Figure 1. The integrated flux of this line calculated from the best-fit function is $0.0652 \pm 0.0175 \text{ Jy km s}^{-1}$, indicating that the CO(6–5) emission line of J0235–0532 shows a marginal

detection at the $\simeq 4\sigma$ significance level. Reassuringly the velocity width of the CO line is comparable to those of the previously detected [C II] and [O III] lines (Harikane et al. 2020b). Because the CO(6–5) is not significantly detected for J1211–0118 and J0217–0208 (Figures 1 and 2), we extract their spectra by placing a beam aperture based on the coordinates of their rest UV continuum emission. The upper limits of their CO(6–5) line fluxes are calculated from the square root of the sum of the squared flux density errors in the range of $\pm 250 \text{ km s}^{-1}$ around the expected CO(6–5) frequency from their systemic redshift. The range of $\pm 250 \text{ km s}^{-1}$ is comparable to twice the FWHM of their [O III] and [C II] emission lines (their FWHMs are about $170\text{--}370 \text{ km s}^{-1}$; Table 1 of Harikane et al. 2020b). The integrated emission line flux or the upper limit for each target and the observed FWHM of the detected line are presented in Table 3.

Figure 3 compares the ALMA spectra of our $z = 6$ luminous LBGs around the CO(6–5) emission line with those around the [O III] and [C II] emission lines. Although the S/N of the CO(6–5) line of J0235–0532 is not high, the redshifts based on the CO, [O III], and [C II] lines are broadly consistent with each other. Some previous studies have shown significant velocity shifts between [O III] and [C II] (e.g., BDF-3299 in Carniani et al. 2017; see Hashimoto et al. 2019; Bakx et al. 2020 as counterexamples); our results suggest that the velocity shift in J0235–0532, if any, is smaller than the previous results.

Figure 4 presents the CO(6–5) emission contours of J0235–0532 with the Subaru HSC z -band image probing the rest-frame UV continuum emission. Although the positions of CO(6–5) and UV continuum appear to be slightly offset, this may be caused by the relatively low S/N of the CO emission. We estimate the uncertainties of the CO peak position by running a suite of Monte Carlo simulations in the same way as Harikane et al. (2020b). We add artificial noises to the actual data according to a Gaussian random distribution with a standard deviation equal to the 1σ noise of the data, and remeasure the peak positions one thousand times to estimate the uncertainties of the CO peak position. We find that the CO peak position is consistent with that of the UV continuum within the 2σ uncertainties. In Figure 4, we also present the [C II] and [O III] positions obtained in Harikane et al. (2020b), confirming that the CO peak position is also consistent with those of [C II] and [O III].

For a sanity check of the position of J0235–0532 in the HSC astrometry, which has been calibrated against the Pan-STARRS first data release (DR1) catalog (Chambers et al. 2016), we use nearby ($< 1'$) bright stars whose positions are accurately measured in the Gaia early data release 3 (EDR3) catalog

²² <https://casa.nrao.edu/>

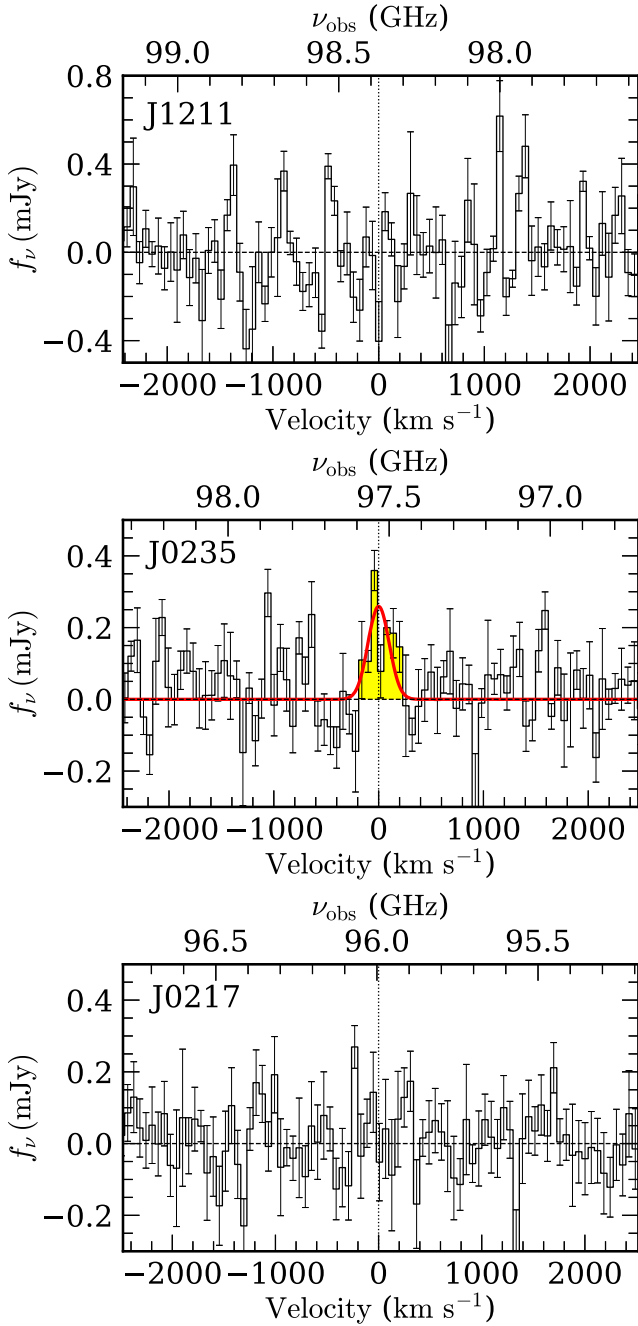


Figure 1. ALMA spectra of J1211–0118 (top), J0235–0532 (middle), and J0217–0208 (bottom) around the redshifted frequency of the CO(6–5) emission line (black histogram) extracted by placing a beam aperture (for details, see the text in Section 4.1). The dotted vertical line corresponds to the systemic redshift determined with the FIR emission lines of [O III] and [C II] (Harikane et al. 2020b). The red curve in the middle panel represents the best-fit Gaussian function to the CO(6–5) emission line.

(Gaia Collaboration et al. 2016, 2021).²³ We confirm that the positional differences of the nearby bright stars between the HSC data and the Gaia EDR3 catalog are only within $<0''.01$ with no systematic offsets, which is consistent with similar comparison results in previous work on a much larger scale (Section 6.3 of Aihara et al. 2019).

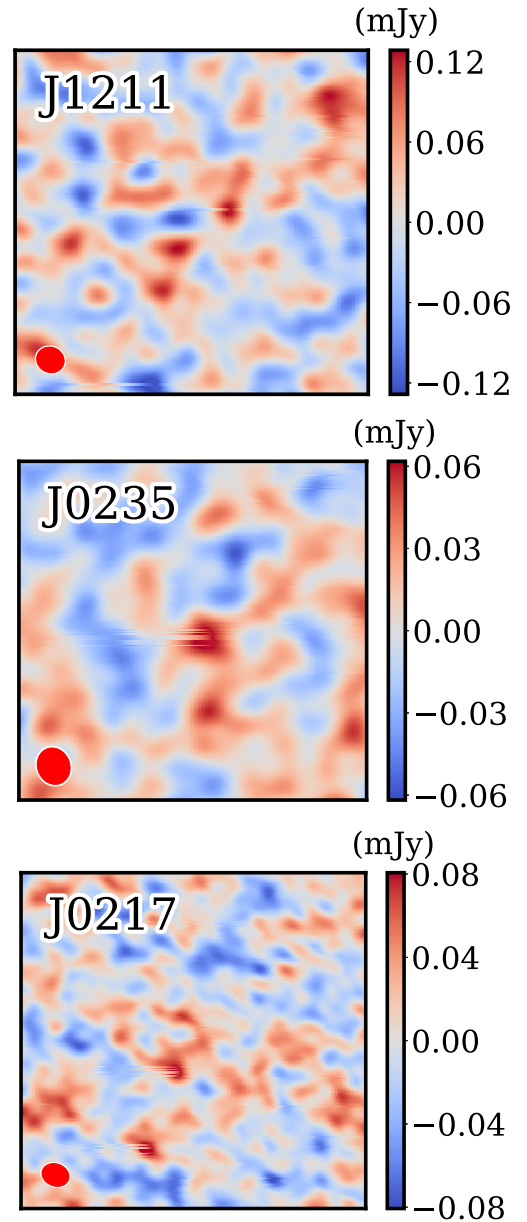


Figure 2. Zeroth-moment images showing the integrated CO(6–5) flux densities of J1211–0118 (top), J0235–0532 (middle), and J0217–0208 (bottom). The synthesized beam is shown in the bottom left corner in each image. The size of each image is $30'' \times 30''$. The range of the color bar for the flux densities corresponds to ± 3 times the standard deviation.

As mentioned above, the significance of the CO(6–5) line from J0235–0532 is only about 4σ . However, the observed CO peak position on the sky is consistent with that of the UV continuum, and the observed CO frequency is also in good agreement with those of the previously detected FIR emission lines; the probability of these events occurring simultaneously by chance is lower than the estimate above. We calculate the combined probability that these three events occur simultaneously by chance based on Fisher’s method (Fisher 1970; see also Finke et al. 2015; Mulders et al. 2018; Kikuchi et al. 2022; cf. Heard & Rubin-Delanchy 2018). First, the probability that the CO detection is a false positive can be calculated from the significance of the CO line from J0235–0532. We obtain a false-positive probability (p -value) of $p_1 \simeq 9.7 \times 10^{-5}$,

²³ <https://gea.esac.esa.int/archive/>

Table 3
Summary of Our Observational Results

	J1211–0118	J0235–0532	J0217–0208
CO(6–5) integrated flux (Jy km s ⁻¹)	<0.0713	0.0652 ± 0.0175	<0.0609
CO(6–5) FWHM (km s ⁻¹)	...	237 ± 51	...
$L_{\text{CO}(6-5)}$ (10 ⁷ L _⊙)	<3.41	2.88 ± 0.773	<3.95
$L'_{\text{CO}(6-5)}$ (10 ⁹ K km s ⁻¹ pc ²)	<3.22	2.72 ± 0.73	<3.74
$f_{\nu,430 \mu\text{m}}$ (μJy)	<52.3	<29.1	<22.1
L_{IR} (10 ¹¹ L _⊙)	3.6 ^{+34.4} _{-1.9}	5.8 ^{+19.4a} _{-5.8}	2.0 ^{+5.9} _{-0.3}
T_{dust} (K)	40 ⁺⁴⁴ ₋₁₄	50–80 (fixed)	31 ⁺²⁶ ₋₉
$f_{\text{CMB}}^{\text{CO}(6-5)}$	0.72	0.79–0.89	0.55
SFR _{IR} (M _⊙ yr ⁻¹)	39 ⁺³⁷⁵ ₋₂₁	63 ^{+211a} ₋₆₃	22 ⁺⁶⁴ ₋₃
SFR _{tot} (M _⊙ yr ⁻¹)	88 ⁺³⁷⁵ ₋₂₁	112 ⁺²¹¹ ₋₆₄	98 ⁺⁶⁵ ₋₅
M_{gas} (10 ¹⁰ M _⊙)	<8.99	7.59 ± 4.74	<10.4
Σ_{SFR} (M _⊙ yr ⁻¹ kpc ⁻²)	9.6 ^{+41.5} _{-2.3}	18.9 ^{+35.6} _{-10.7}	48.2 ^{+31.6} _{-2.5}
Σ_{gas} (10 ³ M _⊙ pc ⁻²)	<9.9	12.8 ± 8.0	<5.1
f_{gas}^b	<0.59	0.55 ^{+0.12} _{-0.23}	<0.46
t_{dep} (Gyr)	<1.02	0.68 ^{+0.90} _{-0.47}	<1.06

Notes. The upper limits are 3σ .

^a These values are the 3σ upper limits when $T_{\text{dust}} = 50$ K, and the upper error takes into account the case when $T_{\text{dust}} = 80$ K. For details, see the text in Section 4.2.

^b The quoted uncertainties in the gas fraction do not include the systematic uncertainty associated with the stellar mass estimates.

assuming that the flux measurement errors follow a Gaussian distribution. Second, the probability that the CO peak position is consistent with the previously detected source position can be calculated from the ratio of the area corresponding to the 2σ range to that of the obtained ALMA data. The p -value for this event is estimated to be $p_2 \simeq 7.3 \times 10^{-4}$. Third, the probability that the detected line frequency coincides with those of the previously detected FIR lines can be calculated from the ratio of twice the FWHM frequency range to that of the four SPWs. The p -value for this event is estimated to be $p_3 \simeq 2.1 \times 10^{-2}$. From these individual p -values, we calculate a test statistic (TS) for the combined probability,

$$\text{TS} = -2 \sum_{i=1}^k \ln p_i, \quad (1)$$

where $k = 3$ in this case. By comparing this TS with the χ^2 distribution with $2k$ degrees of freedom, χ_{2k}^2 , we obtain a combined p -value $p_{\text{com}} \simeq 3.4 \times 10^{-7}$ from

$$p_{\text{com}} = \int_{\text{TS}}^{\infty} \chi_{2k}^2(x) dx. \quad (2)$$

We then solve the equation

$$p_{\text{com}} = \int_{S/N_{\text{com}}}^{\infty} \frac{1}{\sqrt{2\pi}} \exp\left(-\frac{x^2}{2}\right) dx, \quad (3)$$

to obtain an equivalent Gaussian standard deviation of $S/N_{\text{com}} \simeq 5.0$ as the combined significance. In this paper, this signal for J0235–0532 is regarded as the CO(6–5) line. However, because the combined significance is still not very high, it is necessary to secure a firm detection of this CO line with follow-up observations.

Although the CO peak position is consistent with that of the UV continuum, the apparent offset (with large uncertainties) might indicate a hint of photoevaporation of photodissociation regions (PDRs; e.g., Carniani et al. 2017; Decataldo et al. 2017; Vallini et al. 2017). A partial displacement between the UV continuum tracing H II regions and CO(6–5) emission tracing dense clumps within giant molecular clouds (GMCs; e.g., McKee & Ostriker 2007) is expected when PDRs are photoevaporated. (For details, see discussion in Vallini et al. 2017.) This scenario can be verified by observing the CO emission from J0235–0532 with a higher S/N and better resolution.

From the integrated CO(6–5) emission line flux, we obtain the CO(6–5) luminosity in units of L_{\odot} by using Equation (18) of Casey et al. (2014). We also calculate the CO(6–5) luminosity in units of $\text{K km s}^{-1} \text{pc}^2$ defined by Equation (19) of Casey et al. (2014). These equations are presented in Appendix A. In these calculations, the effect of the cosmic microwave background (CMB) is taken into account by dividing the observed integrated flux by a factor of f_{CMB} (da Cunha et al. 2013),

$$f_{\text{CMB}} = 1 - \frac{B_{\nu}[T_{\text{CMB}}(z)]}{B_{\nu}[T_{\text{exc}}]}, \quad (4)$$

where B_{ν} is the Planck function, $T_{\text{CMB}}(z) = 2.73(1+z)$ K is the temperature of the CMB, and T_{exc} is the excitation temperature of the CO(6–5) transition. Assuming local thermal equilibrium (LTE), T_{exc} is equal to the kinetic temperature of the gas, T_{kin} , and then to the dust temperature, T_{dust} , i.e., $T_{\text{exc}} = T_{\text{kin}} = T_{\text{dust}}$.²⁴ Here we use T_{dust} estimated in Section 4.2. The obtained CO luminosities or upper limits, as well as the f_{CMB} values, are presented in Table 3.²⁵ Note, as a caveat, that this prescription assumes a uniform kinetic temperature for CO- and dust continuum-emitting regions. However, in reality, PDRs have a kinetic temperature profile that depends on the radiation field and the gas density. If the kinetic temperature of the CO-emitting regions is higher than adopted here, T_{exc} would be higher and thus f_{CMB} would be higher (Section 2.4 of Vallini et al. 2015; see also Section 4.3 of Vallini et al. 2018). In this sense, the da Cunha et al. (2013) prescription may provide a pessimistic estimate of the fraction of the intrinsic flux observed.

4.2. Dust Continuum Emission

The dust continuum emission from our $z = 6$ luminous LBGs at $\lambda_{\text{obs}} \simeq 3$ mm ($\lambda_{\text{rest}} \simeq 430 \mu\text{m}$) is not significantly detected. The 3σ upper limits of their dust continuum flux densities are $52.3 \mu\text{Jy}$ for J1211–0118, $29.1 \mu\text{Jy}$ for J0235–0532, and $22.1 \mu\text{Jy}$ for J0217–0208. Their dust continuum emission maps are presented in Appendix C.

²⁴ Note that, even in the case of non-LTE, if the gas temperature and density are relatively high, the CMB effect for the CO(6–5) line is comparable to that in the LTE case (see the non-LTE example with $T_{\text{kin}} = 40$ K and the number density of H₂ molecules $n_{\text{H}_2} = 10^{4.2} \text{cm}^{-3}$ in Figure 10 of da Cunha et al. 2013; cf. Figure 6 of da Cunha et al. 2013).

²⁵ Because no dust continuum is detected in J0235–0532 in our data and the previous data (Harikane et al. 2020b), the obtained constraint on T_{dust} is not stringent. We thus consider the T_{dust} uncertainty when we obtain the uncertainties of the physical quantities of J0235–0532 that are related to T_{dust} such as the IR luminosity and the CO luminosity. For details, see Section 4.2.

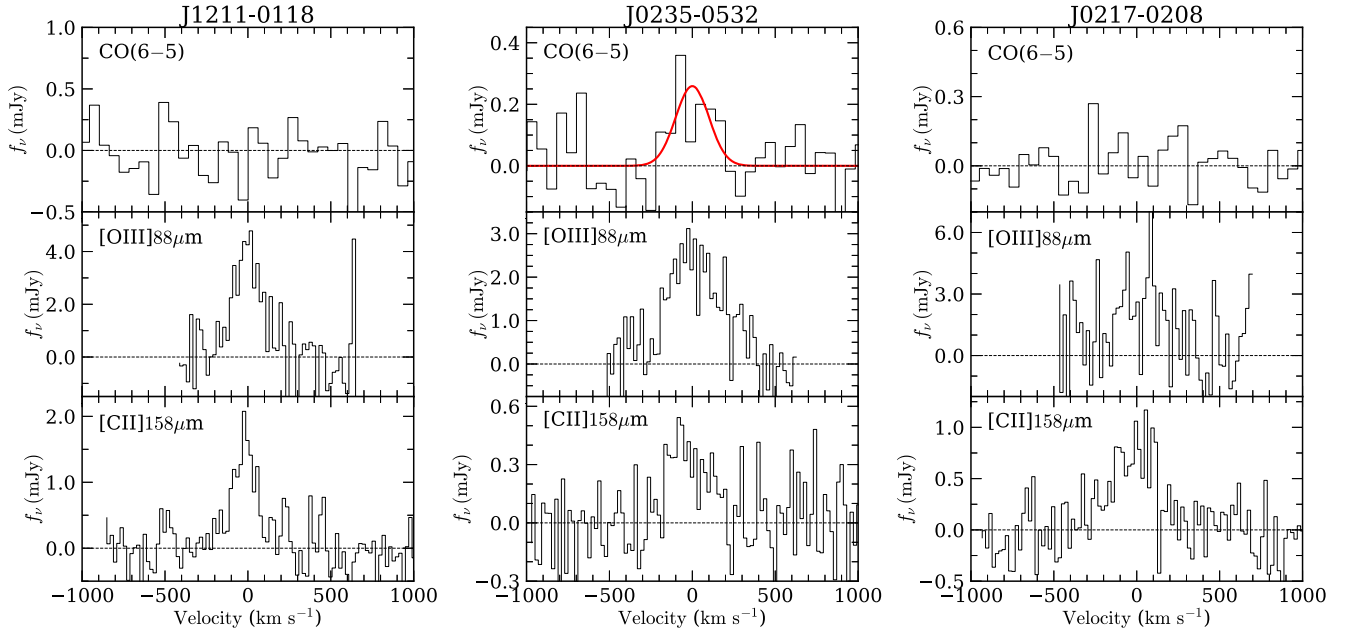


Figure 3. ALMA spectra of J1211–0118 (left), J0235–0532 (center), and J0217–0208 (right) around CO(6–5), [O III] 88 μm , and [C II] 158 μm from top to bottom. The CO spectra are the same as the ones shown in Figure 1, but the velocity range is limited to $[-1000 \text{ km s}^{-1}, 1000 \text{ km s}^{-1}]$. The spectra for [O III] 88 μm and [C II] 158 μm have been obtained in Harikane et al. (2020b).

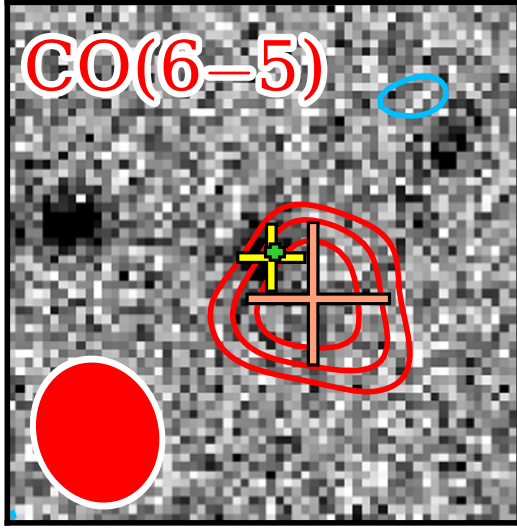


Figure 4. CO(6–5) contours for J0235–0532. The red (blue) contours are multiples of 0.5σ (-0.5σ) starting at 2σ (-2σ). The synthesized beam is shown in the bottom left corner. The gray background is the Subaru HSC z -band image of J0235–0532 that captures the rest-frame UV continuum emission. The positions of the CO(6–5) and UV continuum emission are consistent within the large uncertainties (light red cross) estimated from the Monte Carlo simulations (for details, see the text in Section 4.1). The yellow and green crosses denote the positions of the [C II] and [O III] emission, respectively, and the sizes of the crosses are their uncertainties (Harikane et al. 2020b), which are also consistent with that of CO(6–5). The size of the image is $10'' \times 10''$.

In order to characterize the properties of their dust continuum emission, we combine our ALMA results at $\lambda_{\text{rest}} \simeq 430 \mu\text{m}$ with the results of Harikane et al. (2020b) at shorter wavelengths of $\lambda_{\text{rest}} \simeq 90\text{--}160 \mu\text{m}$, and fit modified blackbody spectral energy distributions (SEDs) to the observed flux densities by varying T_{dust} and L_{IR} . We calculate the intrinsic dust continuum flux densities of a modified blackbody SED by using Equation (A5), and then obtain the expected dust continuum flux densities of the modified blackbody, $f_{\nu}^{(\text{exp})}$,

from $f_{\nu}^{(\text{int})}$ by considering the CMB heating and attenuation effects based on the prescription of da Cunha et al. (2013) in the same way as described in Section 4.1. In the dust continuum SED fitting, we require that T_{dust} be higher than the CMB temperature at the redshift of the galaxy ($\sim 20 \text{ K}$ at $z \sim 6$).

Figure 5 shows the results of fitting the modified blackbody SED to the observed SEDs. For J1211–0118 and J0217–0208, modified blackbody SEDs fit well with the observed SEDs. The best-fit IR luminosities and dust temperatures are $(L_{\text{IR}}, T_{\text{dust}}) = (3.6^{+34.4}_{-1.9} \times 10^{11} L_{\odot}, 40^{+44}_{-14} \text{ K})$ for J1211–0118 and $(2.0^{+5.9}_{-0.3} \times 10^{11} L_{\odot}, 31^{+26}_{-9} \text{ K})$ for J0217–0208, which are consistent with the results of Harikane et al. (2020b). Considering the large T_{dust} uncertainties, the reason why the CO emission lines are not detected for these targets may be that the CMB attenuation effect for these targets is relatively large (f_{CMB} is small) due to low T_{dust} . Because our observations only add an upper limit to the observed SEDs on the longer wavelength side of the SED peak, the parameter constraints do not become stronger than the previous work. The two parameters of L_{IR} and T_{dust} are still degenerate, which will be greatly improved if deep observations of the dust continuum emission at shorter wavelengths than the SED peak are conducted. Note that another method has been proposed recently to determine T_{dust} and the dust mass assuming dust to be in radiative equilibrium if the source size of dust continuum emission is obtained (Inoue et al. 2020). Alternatively, it would be possible to have independent estimates of L_{IR} and T_{dust} , as well as the dust mass, based on the dust continuum and [C II] line luminosities by adopting the method recently presented in Sommovigo et al. (2021).

For J0235–0532, although the allowed parameter ranges are determined based on the upper limits of the flux densities, the constraints obtained on L_{IR} and T_{dust} are not stringent. Following Harikane et al. (2020b), we adopt $T_{\text{dust}} = 50 \text{ K}$ for this galaxy without continuum detection as a fiducial value (see also Hashimoto et al. 2019) for comparisons with previous

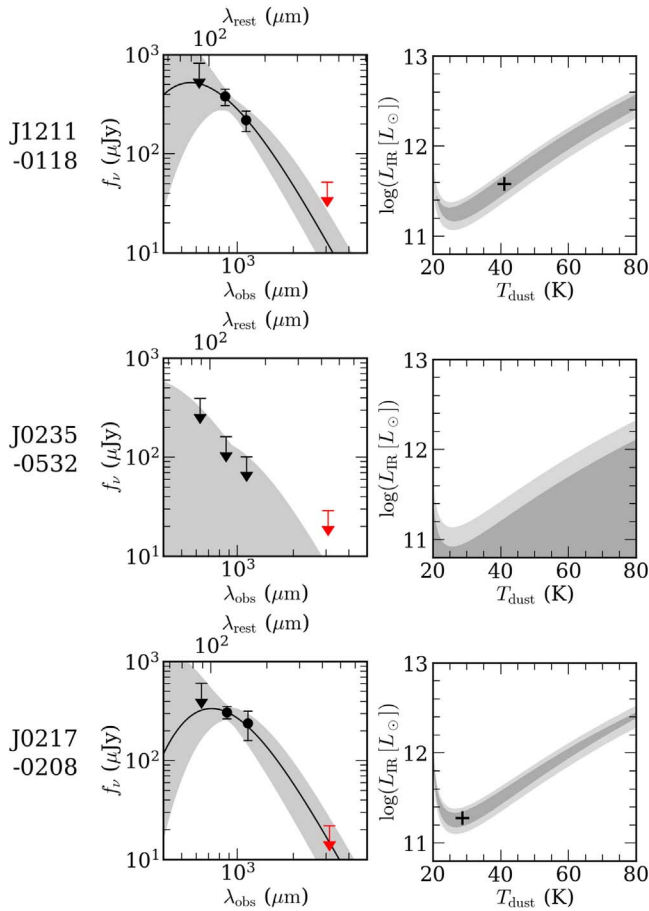


Figure 5. Left: dust continuum SEDs of our $z=6$ luminous LBGs, J1211–0118, J0235–0532, and J0217–0208 from top to bottom. The red arrows are the 3σ upper limits on the flux densities obtained in our ALMA observations. The black circles and downward arrows denote the observed flux densities and 3σ upper limits, respectively, obtained in Harikane et al. (2020b). The black solid curve indicates the best-fit modified blackbody and the gray shade corresponds to the 1σ uncertainties. Right: error contours for the two parameters L_{IR} and T_{dust} in the modified blackbody fitting. The dark and light shades denote the 1σ and 2σ confidence regions, respectively. The black cross corresponds to the best-fit parameters.

studies, which yields a 3σ upper limit of $L_{\text{IR}} < 5.8 \times 10^{11} L_{\odot}$. We also consider the case of a higher dust temperature of $T_{\text{dust}}=80$ K as a systematic uncertainty. This is because J0235–0532 has the highest $[\text{O III}]/[\text{C II}]$ luminosity ratio (Table 1), possibly suggesting a relatively high dust temperature. In fact, previous observations of nearby galaxies have shown that SFGs with higher $[\text{O III}]/[\text{C II}]$ ratios tend to have higher T_{dust} values (Walter et al. 2018), although the $[\text{O III}]/[\text{C II}]$ ratios of their SFGs are not as high as those of J0235–0532. More recently, dust continuum observations of a $z=8.31$ galaxy with a similarly high $[\text{O III}]/[\text{C II}]$ ratio, MACS0416–Y1, have suggested a possibility that its dust temperature may be extremely high, exceeding 80 K, although its physical origin is still under discussion (Bakx et al. 2020). One possible physical explanation for very high dust temperatures is that part of their dust is locked in molecular clouds and/or young star clusters that host active star formation. Based on hydrodynamic simulations, Behrens et al. (2018) have shown that, in such a situation, dust is heated by the strong interstellar radiation fields and can show a very high temperature, efficiently emitting FIR continuum, which can explain the high FIR luminosity without invoking

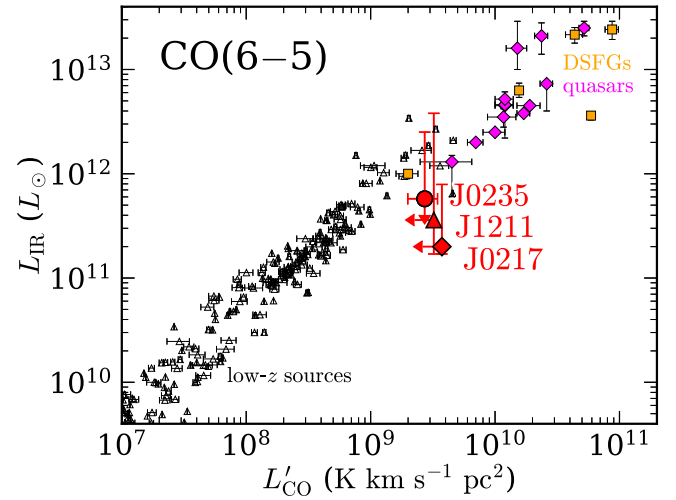


Figure 6. IR luminosity integrated over the wavelength range of 8–1000 μm , L_{IR} , vs. CO(6–5) luminosity in units of $\text{K km s}^{-1} \text{pc}^2$, L'_{CO} . The red circle is our ALMA result for a luminous LBG at $z=6$, J0235–0532, whose CO(6–5) emission shows the 4σ significance level, with L_{IR} and L'_{CO} in the case of $T_{\text{dust}}=50$ K (Hashimoto et al. 2019; Harikane et al. 2020b). The upper error bar along the y-axis for J0235–0532 considers the case of a higher dust temperature of $T_{\text{dust}}=80$ K. The red triangle and diamond are also our ALMA results for the other luminous LBGs at $z=6$, J1211–0118 and J0217–0208, respectively, which show no significant CO(6–5) detection. The red arrows correspond to the 3σ upper limits. The orange squares are high- z DSFGs (Riechers et al. 2010; Strandet et al. 2017; D’Odorico et al. 2018; Apostolovski et al. 2019; Casey et al. 2019) and the magenta diamonds are high- z quasars (Wang et al. 2010, 2011, 2016; Venemans et al. 2017a; Carniani et al. 2019) at $z \sim 5$ –7. The black triangles are nearby galaxies, Seyfert galaxies, and (U) LIRGs at low redshifts ($z < 0.1$) compiled by Liu et al. (2015).

mechanisms for massive dust production at high redshifts (see also, e.g., Arata et al. 2019; Sommovigo et al. 2020). The case of higher T_{dust} for J0235–0532 yields a more conservative upper limit of $L_{\text{IR}} < 2.5 \times 10^{12} L_{\odot}$ (3σ).

In Figure 6, we compare the CO(6–5) and IR luminosities of our luminous LBGs at $z=6$ with those of nearby sources at $z < 0.1$ (Liu et al. 2015) as well as dusty star-forming galaxies (DSFGs; Riechers et al. 2010; Strandet et al. 2017; D’Odorico et al. 2018; Apostolovski et al. 2019; Casey et al. 2019) and quasars (Wang et al. 2010, 2011, 2016; Venemans et al. 2017a; Carniani et al. 2019) at comparable redshifts of $z \sim 5$ –7 to our targets. For nearby sources, the correlation between CO and IR luminosities has been found over a wide luminosity range (Liu et al. 2015), which can be interpreted as an integrated KS relation because the CO and IR luminosities are correlated with gas mass and SFR, respectively (e.g., Magdis et al. 2017). We find that our result for J0235–0532, which is the only one of our targets showing CO(6–5) detection at the $\simeq 4\sigma$ significance level, is broadly consistent with previous results owing to the relatively large uncertainty on the IR luminosity. For J1211–0118 and J0217–0208, whose CO emission is not detected, our results are also consistent with previous results. In other words, the obtained upper limits on CO luminosity for these two sources are not deep enough to know whether they deviate from the correlation between L'_{CO} and L_{IR} seen in low- z sources or not, which can be distinguished by much deeper CO observations.

Note that the excitation of the CO spectral line energy distribution (SLED) varies as a function of gas density, radiation field, Mach number within GMCs, and presence of shocks (e.g., Vallini et al. 2018; Pensabene et al. 2021), and thus the CO(6–5) emission line, which traces dense gas with

critical density of $n_{\text{crit}} = 2.9 \times 10^5 \text{ cm}^{-3}$, would trace a fraction of the total molecular gas, i.e., dense clumps within GMCs. Thus, the relation between $L'_{\text{CO}(6-5)}$ and L_{IR} would not be entirely related to the $M_{\text{gas}}\text{-SFR}$ relation, and the interpretation as an integrated version of the KS relation could be partially hampered. In Sections 5.2 and 5.3, we convert $L'_{\text{CO}(6-5)}$ to $L'_{\text{CO}(1-0)}$ by adopting the average CO SLED for SFGs at lower redshifts to obtain the estimates of gas mass and gas surface density from $L'_{\text{CO}(1-0)}$, and compare them with the KS relation found in the local universe, although the systematic uncertainties in such conversions are not small (Section 5.4).

5. Discussion

In this section, first we discuss physical origins for the relatively strong CO emission of J0235–0532 compared to the other two targets based on comparisons with a PDR model and previous results. Next, we derive the constraints on total gas mass from our CO results for the $z = 6$ luminous LBGs, and present comparisons of their gas surface densities with previous results. Finally, we caution that the obtained constraints on gas mass still have substantial systematic uncertainties. Note that we also present other gaseous properties of gas fraction and gas depletion timescale and compare them with previous results in Appendix D.

5.1. Physical Reasons for the Luminous CO(6–5) Emission in J0235–0532

In this study, we have observed CO(6–5) emission for the three luminous LBGs at $z = 6$ with comparable total SFRs of $\sim 100 M_{\odot} \text{ yr}^{-1}$. As a result, CO(6–5) is marginally detected in J0235–0532 at the $\simeq 4\sigma$ significance level, but not in the other two LBGs. In this section, we discuss physical reasons for this difference.

Because the [C II] emission has also been detected for these LBGs in Harikane et al. (2020b), we calculate the line ratio of CO(6–5) to [C II] as well as the ratio of the [C II] to IR luminosity, which are useful for obtaining constraints on the physical properties of PDRs in galaxies such as the density of hydrogen nuclei, n_{H} , and the incident far-ultraviolet (FUV) radiation field, U_{UV} , with 6–13.6 eV based on comparisons with theoretical models for PDRs. For the PDR modeling, we use the Photodissociation Region Toolbox (PDRT; Kaufman et al. 1999, 2006; Pound & Wolfire 2008),²⁶ which calculates various line and continuum intensity ratios for combinations of n_{H} and U_{UV} by solving for the equilibrium chemistry, thermal balance, and radiation transfer through a PDR layer in a self-consistent way. Specifically, we use the wk2006 model of the PDRT with solar metallicity for comparisons with previous results.

Because the [C II] emission comes from not only PDRs but also H II regions, we need to subtract the contribution of [C II] emission from H II regions for comparisons with the results of the PDRT calculation. For this purpose, we refer to Figure 9 of Cormier et al. (2019), which presents the dependence of the fraction of [C II] emission from H II regions, $f_{[\text{C II}]}^{(\text{ion})}$, on gas-phase metallicity (see also Figure 4 of Croxall et al. 2017; Sutter et al. 2019; Rybak et al. 2021; see also theoretical results such as Katz et al. 2017; Olsen et al. 2017; Ferrara et al. 2019; Pallottini et al. 2019). Based on analyses of interstellar medium

absorption lines detected in the stacked spectrum of $z \sim 6$ luminous LBGs with $M_{\text{UV}} \simeq -23$ mag including one of our targets, J1211–0118, Harikane et al. (2020a) have found that their gas-phase metallicity is close to solar.²⁷ By combining these two previous results, $f_{[\text{C II}]}^{(\text{ion})}$ of our $z = 6$ luminous LBGs would be about $f_{[\text{C II}]}^{(\text{ion})} \simeq 0.3$. Because the observed $f_{[\text{C II}]}^{(\text{ion})}$ values have a scatter of $\simeq 0.1\text{--}0.2$, here we consider it as a systematic uncertainty. We also apply a factor-of-two correction for the observed CO flux considering line luminosity from both sides of each optically thick cloud for comparisons with the results of the PDRT calculation, as suggested by Kaufman et al. (1999) (see also Wang et al. 2016; Rybak et al. 2019; Shao et al. 2019).

Because the $f_{[\text{C II}]}^{(\text{ion})}$ values are correlated with the [C II]/[N II] 122 μm luminosity ratio as presented in Figure 10 of Cormier et al. (2019), we can also evaluate $f_{[\text{C II}]}^{(\text{ion})}$ from [C II]/[N II]. However, the [N II] emission has not been detected in any of our targets (Harikane et al. 2020b), and the lower limits on the [C II]/[N II] ratios are not so stringent. Calculating the 3σ lower limits on the [C II]/[N II] ratios based on Table 1 of Harikane et al. (2020b), we obtain $L_{[\text{C II}]} / L_{[\text{N II}]} > 0.36\text{--}2.3$. We confirm that the expected ranges of the $f_{[\text{C II}]}^{(\text{ion})}$ values from the lower limits of the [C II]/[N II] ratios are consistent with those expected from the gas metallicity.

By taking account of these points, in the top left panel of Figure 7, we compare our ALMA results for $L_{\text{CO}(6-5)} / L_{[\text{C II}]}$ versus $L_{[\text{C II}]} / L_{\text{IR}}$ with the results of the PDRT calculation. Because the PDRT does not include the CMB temperature, the observed CO and IR luminosities are corrected for the CMB effect (Section 4).²⁸ In the same way as in Figure 6, we adopt $T_{\text{dust}} = 50$ K for J0235–0532 as a fiducial value and consider up to $T_{\text{dust}} = 80$ K as a systematic uncertainty, yielding a conservative lower limit of $L_{[\text{C II}]} / L_{\text{IR}}$. We find that the n_{H} value of J0235–0532 is higher than those of J1211–0118 and J0217–0208. Because we only obtain the lower limit for the $L_{[\text{C II}]} / L_{\text{IR}}$ ratio of J0235–0532 due to the nondetection of the dust continuum emission, it is unclear whether the incident FUV radiation is stronger in J0235–0532 than in the others or not.

For comparisons of the n_{H} and U_{UV} values of our $z = 6$ luminous LBGs with those of other sources at lower redshifts, in the top right panel of Figure 7, we show previous observation results for $L_{\text{CO}(1-0)} / L_{[\text{C II}]}$ versus $L_{[\text{C II}]} / L_{\text{IR}}$ of luminous infrared galaxies (LIRGs), ultraluminous infrared galaxies (ULIRGs; Rosenberg et al. 2015), quasars (Benford et al. 1999; Maiolino et al. 2005; Iono et al. 2006; Wagg et al. 2012, 2014; Leipski et al. 2013; Stefan et al. 2015; Wang et al. 2016; Venemans et al. 2017b; compiled by Shao et al. 2019), local SFGs such as spiral galaxies, and Galactic star-forming regions (Stacey et al. 1991), as well as the results of the PDRT model calculation. For easier comparison, the bottom panel of Figure 7 is the same as the top left panel but with the colored shaded regions that roughly correspond to the locations of low- z sources in the previous work with CO(1–0) observations shown in the top right panel. We find that the relatively high n_{H}

²⁷ This result is consistent with our use of the wk2006 model of the PDRT with solar metallicity.

²⁸ Although we compare the observed results corrected for the CMB effect with the results of the PDRT calculation, the PDRT calculation with the consideration of the CMB effect may change the shape of the diagnostic (M. Wolfire 2022, private communication). We need to check this point when the theoretical models are updated in the future.

²⁶ <http://dustem.astro.umd.edu/index.html>

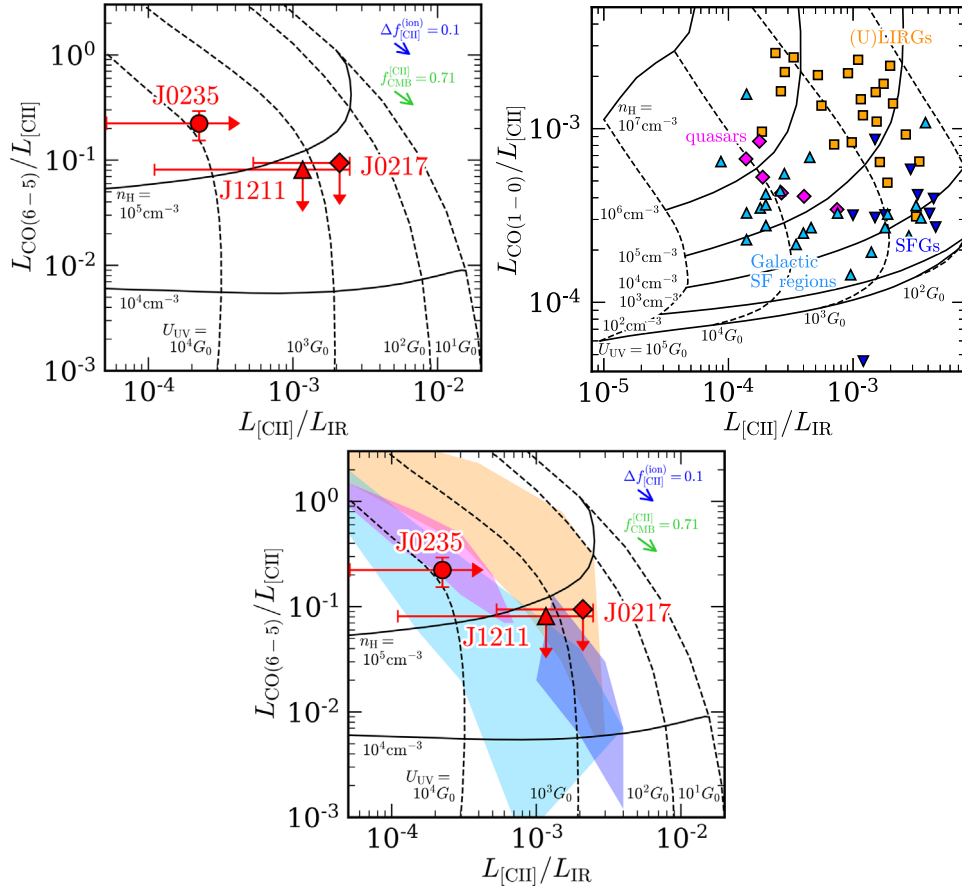


Figure 7. Top left: $L_{\text{CO}(6-5)}/L_{[\text{C II}]}$ vs. $L_{[\text{C II}]/L_{\text{IR}}}$. The red circle is our ALMA result for a luminous LBG at $z = 6$ with $\simeq 4\sigma$ CO(6–5) detection, J0235–0532, in the case of $T_{\text{dust}} = 50$ K, and the lower error bar along the x-axis considers the higher dust temperature case of $T_{\text{dust}} = 80$ K. The red triangle and diamond are also our ALMA results for the other luminous LBGs at $z = 6$, J1211–0118 and J0217–0208, respectively, which show no significant CO(6–5) detection. The red arrows correspond to the 3σ limits. The solid and dashed curves represent the theoretical calculations with the PDRT with constant densities of hydrogen nuclei, n_{H} , in units of cm^{-3} , and FUV (6–13.6 eV) radiation fields, U_{UV} , in units of the average interstellar radiation field in the vicinity of the Sun, $G_0 = 1.6 \times 10^{-3} \text{ erg s}^{-1} \text{ cm}^{-2}$ (Habing 1968), respectively. The blue arrow in the upper right corner represents the amount of shift when $f_{[\text{C II}]}^{(\text{ion})}$ increases by 0.1. The green arrow in the upper right corner shows the systematic uncertainties of the CMB effect on the [C II] emission (Kohandel et al. 2019). Top right: $L_{\text{CO}(1-0)}/L_{[\text{C II}]}$ vs. $L_{[\text{C II}]/L_{\text{IR}}}$. The orange squares denote LIRGs and ULIRGs (Rosenberg et al. 2015). The blue downward triangles and cyan triangles represent local SFGs and Galactic star-forming regions, respectively (Stacey et al. 1991). The magenta diamonds represent high- z quasars (Benford et al. 1999; Maiolino et al. 2005; Iono et al. 2006; Wagg et al. 2012, 2014; Leipski et al. 2013; Stefan et al. 2015; Wang et al. 2016; Venemans et al. 2017b; compiled by Shao et al. 2019). The solid and dashed curves are the same as in the left panel. In both panels, the CO line luminosities are multiplied by a factor of two as recommended by Kaufman et al. (1999) (for details, see the text in Section 5.1; see also Shao et al. 2019). Bottom: same as the top left panel, but with the colored shaded regions that roughly correspond to the low- z CO(1–0) results presented in the top right panel.

value of J0235–0532, $n_{\text{H}} \gtrsim 10^5 \text{ cm}^{-3}$ depending on U_{UV} , is consistent with those of LIRGs and ULIRGs with relatively low n_{H} values in that population, as well as with those of quasars and Galactic star-forming regions with high n_{H} and U_{UV} values considering the case of high T_{dust} . We also find that J1211–0118 and J0217–0208, likely showing moderate U_{UV} values with n_{H} upper limits around 10^5 cm^{-3} , are consistent with nuclear regions of local SFGs and Galactic star-forming regions with relatively low n_{H} values.

It should be noted that there are two systematic uncertainties in this comparison. One is related to $f_{[\text{C II}]}^{(\text{ion})}$. As mentioned above, the relation between $f_{[\text{C II}]}^{(\text{ion})}$ and metallicity has a scatter of about 0.1–0.2 (e.g., Figure 9 of Cormier et al. 2019). In our $L_{\text{CO}(6-5)}/L_{[\text{C II}]}$ versus $L_{[\text{C II}]/L_{\text{IR}}}$ figures, we show the blue arrow in the upper right corner that corresponds to the amount of shift when $f_{[\text{C II}]}^{(\text{ion})}$ is increased by 0.1. We confirm that this systematic uncertainty does not significantly affect the results. The other systematic uncertainty is the effect of the CMB on the [C II] emission. As discussed in Section 6.1 of Harikane

et al. (2020b), the [C II] emission may also be affected by the CMB attenuation due to the high CMB temperature at $z \sim 6$ (see also González-López et al. 2014; Lagache et al. 2018; Laporte et al. 2019). Figure 1 of Kohandel et al. (2019) shows the CMB suppression effect of the [C II] emission with different gas temperatures as a function of gas number density. Although only upper limits are derived for n_{H} of J1211–0118 and J0217–0208, with a conservative gas density value of 10^4 cm^{-3} , we obtain the effect of the CMB on the [C II] emission line flux of $f_{\text{CMB}}^{[\text{C II}]} = 0.71\text{--}0.86$ at 30–40 K (Kohandel et al. 2019; see also Pallottini et al. 2015; Vallini et al. 2015), which is comparable to the dust temperature. If the gas density and/or the gas temperature is higher, then the CMB effect is smaller, suggesting that the impact of this systematic uncertainty is comparable to or smaller than that of the $f_{[\text{C II}]}^{(\text{ion})}$ scatter.

There is another noticeable difference between J0235–0532 and the other two LBGs. J0235–0532 has the highest [O III]/[C II] luminosity ratio ($[\text{O III}]/[\text{C II}] = 8.9 \pm 1.7$) among our targets, as shown in Figure 5 of Harikane et al. (2020b). In the first place, these three $z = 6$ LBGs have significantly higher

[O III]/[C II] ratios than $z \sim 0$ galaxies with comparable total SFRs.²⁹ Harikane et al. (2020b) have discussed the physical reason for this based on comparisons with the results of model calculations for both H II regions and PDRs with CLOUDY (Ferland et al. 1998, 2017) and concluded that high ionization parameters and/or low PDR covering fractions can explain high- z galaxy results including the high [O III]/[C II] ratios and low $L_{[\text{C II}]}/\text{SFR}$ ratios. Harikane et al. (2020b) have also found that high n_{H} , low C/O ratios, and the CMB attenuation effect can reproduce a part of the high- z galaxy results.

Because the CO emission originates from different regions from [O III]-/[C II]-emitting regions (e.g., Figure 31.2 of Draine 2011), it is difficult to make a direct comparison between our results and the results of Harikane et al. (2020b). The least we can say is that our results suggest a relatively high n_{H} in PDRs of J0235–0532 compared to the other two LBGs, which would be consistent with the results of Harikane et al. (2020b), although in their study it is not enough to explain the high- z galaxy results. In addition, U_{UV} of J0235–0532 may be higher than those of the other two LBGs, which would be consistent with the high [O III]/[C II] ratio and thus the relatively high ionization parameter, although deeper dust continuum observations are required for constraining $L_{[\text{C II}]} / L_{\text{IR}}$ to reach a conclusion on this point.

Interestingly, this is in line with what is expected from theoretical models. The high- J CO lines trace regions of relatively high density more directly connected to star formation. At such a high density, the self-shielding effect prevents the dissociation of molecules and at the same time the high temperature produced by the strong UV radiation suggested from the high [O III]/[C II] ratio is expected to boost the high- J CO emission (Vallini et al. 2018). In this case, the dust temperature is also likely to be high (Behrens et al. 2018). In fact, the dust continuum is not detected only for J0235–0532, which is consistent with the possibility that the dust temperature of J0235–0532 may be very high. To confirm this picture, it would be interesting to carry out deep observations to detect high- J CO emission from SFGs with high [O III]/[C II] ratios and/or high T_{dust} , such as MACS1149-JD1 at $z = 9.1096$ ([O III]/[C II] $\gtrsim 19$; Hashimoto et al. 2018; Laporte et al. 2019), MACS0416-Y1 at $z = 8.3118$ ([O III]/[C II] = 8.6 ± 2.5 and $T_{\text{dust}} > 80$ K; Tamura et al. 2019; Bakx et al. 2020), and SXDF-NB1006-2 at $z = 7.2120$ ([O III]/[C II] $\gtrsim 10$; Inoue et al. 2016). Note that careful estimates of their [O III]/[C II] luminosity ratios have been provided recently by considering the surface brightness dimming effect (Camiani et al. 2020); they still show relatively high [O III]/[C II] values of 4.2 ± 1.4 for MACS1149-JD1, 8 ± 2 for MACS0416-Y1, and 4.3 ± 1.4 for SXDF-NB1006-2. We confirm that these sources also have high [O III]/[C II] surface brightness ratios (Vallini et al. 2021).

²⁹ It should be noted that the [O III]/[C II] luminosity ratio of some high- z galaxies can be overestimated because the [C II]-emitting region of ALMA-detected high- z galaxies is typically about 2–3 times more extended than the [O III] and UV continuum-emitting regions (Camiani et al. 2020; see also Fujimoto et al. 2019, 2020; Herrera-Camus et al. 2021). To capture the extended [C II] emission, Harikane et al. (2020b) have calculated the total line fluxes with a large ($2''$ radius) aperture (see their Sections 4.1 and 6.1). Recently, Vallini et al. (2021) have proposed that the [O III]/[C II] surface brightness ratio is also useful to overcome this issue. We confirm that our $z = 6$ luminous LBGs also have high [O III]/[C II] surface brightness ratios and J0235–0532 shows the highest value among them (Vallini et al. 2021; see also Camiani et al. 2020).

5.2. Constraints on Gas Mass

We constrain molecular gas masses in our $z = 6$ luminous LBGs based on our CO(6–5) results, although the systematic uncertainties are not small, particularly in the CO SLED, which has not been investigated well for SFGs at high redshifts. Here we present conservative constraints on molecular gas masses in our targets by taking account of such uncertainties and compare with previous results for lower- z sources.

The total gas mass for molecular clouds, M_{gas} , can be estimated from the CO(1–0) luminosity in units of $\text{K km s}^{-1} \text{ pc}^2$, $L'_{\text{CO}(1-0)}$, by using Equation (4) of Solomon & Vanden Bout (2005),

$$M_{\text{gas}} = \alpha_{\text{CO}} L'_{\text{CO}(1-0)}, \quad (5)$$

where α_{CO} is the conversion factor from $L'_{\text{CO}(1-0)}$ to M_{gas} . We assume a fixed value of $\alpha_{\text{CO}} = 4.5 M_{\odot} (\text{K km s}^{-1} \text{ pc}^2)^{-1}$,³⁰ which is consistent with previous results for the Milky Way (Bolatto et al. 2013), $z \sim 1$ –2 SFGs (Daddi et al. 2010; Carilli & Walter 2013), and even an LBG at $z = 5.7$ (HZ10; Pavese et al. 2019).³¹ The $L'_{\text{CO}(1-0)}$ values of our $z = 6$ luminous LBGs can be estimated from $L'_{\text{CO}(6-5)}$ by using the average CO SLED for SFGs. Specifically, we assume that the integrated flux of CO(6–5) is comparable to that of CO(5–4), i.e., $L'_{\text{CO}(6-5)} \simeq L'_{\text{CO}(5-4)}$, and adopt the average integral CO line flux ratio of $L'_{\text{CO}(5-4)} / L'_{\text{CO}(1-0)} \simeq 5.8 \pm 3.3$, which is measured for $z \sim 1$ –2 SFGs (Daddi et al. 2015). The large uncertainty of $L'_{\text{CO}(5-4)} / L'_{\text{CO}(1-0)}$ is estimated from the standard deviation of the integrated CO flux ratios of the $z \sim 1$ –2 SFGs reported in Daddi et al. (2015).³² We then calculate $L'_{\text{CO}(1-0)}$ ³³ and obtain M_{gas} constraints as summarized in Table 3.

Note that Zanella et al. (2018) have reported a linear correlation between the [C II] luminosity and the gas mass for $z \sim 2$ SFGs and obtained a conversion factor from the [C II] luminosity and the gas mass, $\alpha_{[\text{C II}]} = 31 M_{\odot} L_{\text{[C II]}}^{-1}$. By adopting this conversion factor, we estimate the gas mass of J0235–0532 from the [C II] luminosity to be only about $1.3 \times 10^{10} M_{\odot}$, which is significantly smaller than that obtained from the CO luminosity. This may suggest that the conversion factor $\alpha_{[\text{C II}]}$ or α_{CO} for high- z luminous LBGs is different from those at low redshifts, or that the CO SLED is different from those for $z \sim 1$ –2 SFGs, although it is difficult to clarify these possibilities with the currently available data. In this study, we adopt the estimates based on the CO luminosity, because it

³⁰ The systematic uncertainties related to this conversion factor are discussed in Section 5.4.

³¹ Pavese et al. (2019) have estimated the total gas mass by subtracting the contribution of stars and dark matter masses from the dynamical mass measured with the significantly detected [C II] line, and obtained the α_{CO} value from the ratio of the estimated total gas mass to the CO luminosity. They have found that the obtained α_{CO} value is $\alpha_{\text{CO}} = 4.2_{-1.7}^{+2.2} M_{\odot} (\text{K km s}^{-1} \text{ pc}^2)^{-1}$, which is consistent with that of the Milky Way, although the uncertainty is not small.

³² Although here we consider the standard deviation of the previous observation results, the uncertainties of the CO SLEDs may be much larger. The details of this point are presented in Section 5.4.

³³ The CO(1–0) luminosity is calculated from

$$L'_{\text{CO}(1-0)} = \frac{L_{\text{CO}(1-0)}}{L_{\text{CO}(6-5)}} \left(\frac{\nu_{\text{CO}(6-5)}^{\text{(rest)}}}{\nu_{\text{CO}(1-0)}^{\text{(rest)}}} \right)^2 L'_{\text{CO}(6-5)}, \quad (6)$$

where $\nu_{\text{CO}(1-0)}^{\text{(rest)}} = 115.27 \text{ GHz}$.

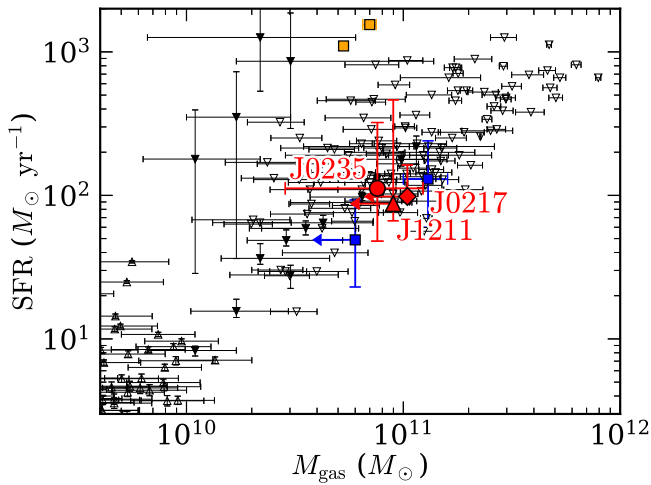


Figure 8. SFR vs. M_{gas} . The red circle is our ALMA result for a luminous LBG at $z = 6$ with $\approx 4\sigma$ CO(6–5) detection, J0235–0532, in the case of $T_{\text{dust}} = 50$ K and $\text{SFR}_{\text{tot}} = \text{SFR}_{\text{UV}} + \text{SFR}_{\text{IR}, 2\sigma}$. The error bar along the y-axis considers the case of a higher dust temperature of $T_{\text{dust}} = 80$ K and the minimum SFR case of $\text{SFR}_{\text{tot}} = \text{SFR}_{\text{UV}}$. Note that, although the intrinsic CO flux and thus the M_{gas} value become somewhat larger with a higher dust temperature, such a systematic uncertainty is much smaller than the uncertainty in the CO flux measurement. The red triangle and diamond are also our ALMA results for the other luminous LBGs at $z = 6$, J1211–0118 and J0217–0208, respectively, which show no significant CO(6–5) detection. The red arrows correspond to the 3σ limits. The blue squares represent the results of LBG-1 and HZ10 from left to right (Pavesi et al. 2019). The blue arrow represents the 3σ limit. The orange squares are the results of AzTEC-3 and CRLE from left to right (Riechers et al. 2010, 2014; Pavesi et al. 2018; see also Pavesi et al. 2019). The black filled downward triangles are the results of SFGs with $M_{\text{star}} > 3 \times 10^{10} M_{\odot}$ at $z \sim 0$ –4 using stacked dust SEDs (Béthermin et al. 2015). The black open downward triangles show the results of SFGs with $M_{\text{star}} > 2 \times 10^{10} M_{\odot}$ at $z \sim 1$ –6 based on submillimeter dust continuum measurements (Scoville et al. 2016). The black open triangles are the results for low- z galaxies at $z = 0.01$ –0.05 (Saintonge et al. 2017).

is more commonly used in previous studies and would thus be more appropriate for comparisons.

In Figure 8, we compare total SFRs and M_{gas} estimates of our $z = 6$ luminous LBGs with dusty starbursts and other SFGs over a wide range of redshifts from $z \sim 0$ to $z \sim 6$ (Béthermin et al. 2015; Scoville et al. 2016; Saintonge et al. 2017) including HZ10, LBG-1, AzTEC-3, and CRLE (Riechers et al. 2010, 2014; Pavesi et al. 2018; see also Pavesi et al. 2019). This figure should be interpreted as an integrated KS relation in a more direct sense than the L_{IR} versus L'_{CO} plot presented as Figure 6 (Section 4.2). Following Kennicutt (1998a), we adopt the molecular gas mass as a proxy for the total gas mass for high-SFR sources including our $z = 6$ luminous LBGs, because such sources in the local universe show that the disks are molecular-dominated (Sanders & Mirabel 1996; see also Kennicutt & De Los Reyes 2021). Because we only obtain the upper limit of SFR_{IR} for J0235–0532, we present the sum of SFR_{UV} and the 2σ upper limit of SFR_{IR} in the case of $T_{\text{dust}} = 50$ K as its total SFR, and consider the higher dust temperature up to $T_{\text{dust}} = 80$ K as well as the minimum SFR case of the SFR_{UV} alone with no SFR_{IR} in the relatively large error bars as systematic uncertainties. We find that our CO-based results for J0235–0532 are in broad agreement with SFGs at various redshifts with similar M_{gas} including HZ10 and LBG-1. J1211–0118 and J0217–0208 are consistent with the previous results with similar SFRs, although their M_{gas} values are upper limits.

5.3. Kennicutt–Schmidt Relation

Although the currently available data for our $z = 6$ luminous LBGs do not resolve their internal structures in detail, we estimate their sizes to calculate their global SFR surface densities and gas surface densities for comparisons with the KS relation for the average surface densities of SFGs in the local universe.

The sizes of star-forming regions of our $z = 6$ luminous LBGs for calculating global SFR surface densities are measured with the HSC z -band images, which trace the rest UV continuum emission. We fit Sérsic profiles (Sersic 1968) to the observed surface brightness distributions by using GALFIT ver. 3.0.5 (Peng et al. 2002, 2010),³⁴ which convolves a galaxy model profile with a point-spread function (PSF) profile and optimizes the fitting parameters based on the Levenberg–Marquardt algorithm for χ^2 minimization (e.g., Press et al. 1992). We use a PSF image for the position of each of our $z = 6$ luminous LBGs downloaded from the PSF picker website of the HSC survey.³⁵ The output parameters include the centroid coordinates of the objects, their total magnitude, the half-light radius along the semimajor axis, the axis ratio, and the position angle. The Sérsic index n is fixed at 1.0.³⁶ We calculate the circularized half-light radius, $r_e = \sqrt{q} r_{e,\text{maj}}$, where q is the axis ratio and $r_{e,\text{maj}}$ is the half-light radius along the semimajor axis, because it is widely used in size measurements in previous high- z galaxy studies (e.g., Mosleh et al. 2012; Newman et al. 2012; Ono et al. 2013; Shibuya et al. 2015; Kawamata et al. 2018). The obtained r_e values are presented in Table 1.

Note that, for J0235–0532, the output axis ratio obtained with GALFIT is enclosed between star symbols, indicating that a numerical convergence issue may have occurred in the fitting for this particular source (for details, see Section 10 of the GALFIT user’s manual). As an alternative method, for J0235–0532, we use SExtractor ver. 2.8.6 (Bertin & Arnouts 1996)³⁷ to calculate the observed half-light radius, $r_e^{(\text{obs})}$, by using circular apertures that contain half of the light from a galaxy, and correct it for the PSF broadening according to

$$r_e = \sqrt{r_e^{(\text{obs})2} - r_{\text{PSF}}^2}, \quad (7)$$

where r_{PSF} is the half-light radius of the PSF image (e.g., Oesch et al. 2010; Holwerda et al. 2020; Bowler et al. 2021; Roberts-Borsani et al. 2022). For this PSF broadening correction, we use the PSF images downloaded from the PSF picker website. The obtained r_e value for J0235–0532 is also presented in Table 1. We also measure the half-light radii of J1211–0118 and J0217–0208 with SExtractor and confirm that the results are consistent with those obtained with GALFIT.

With the obtained r_e values, we define SFR surface density, Σ_{SFR} , as the average SFR in a circular region whose half-light radius is r_e (Equation (A6)). The obtained Σ_{SFR} values are listed in Table 3.

Because the resolution of our ALMA data is not high enough to estimate the sizes of CO-emitting regions, we calculate their gas surface densities by assuming that the sizes of CO-emitting regions are comparable to those of star-forming regions. In fact,

³⁴ <https://users.obs.carnegiescience.edu/peng/work/galfit/galfit.html>

³⁵ <https://hsc-release.mtk.nao.ac.jp/psf/pdr2/>

³⁶ We confirm that the obtained sizes show little difference if we use $n = 1.5$.

³⁷ <https://www.astromatic.net/software/sextractor/>

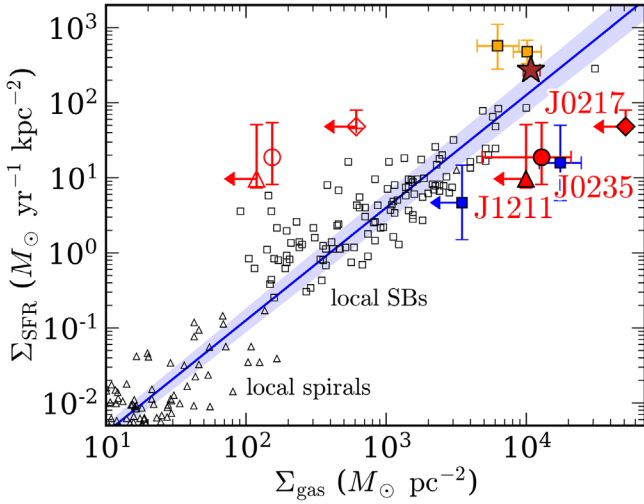


Figure 9. Σ_{SFR} vs. Σ_{gas} . The red filled circle is our ALMA result for a luminous LBG at $z = 6$ with $\sim 4\sigma$ CO(6–5) detection, J0235–0532, in the case of $T_{\text{dust}} = 50$ K and $\text{SFR}_{\text{tot}} = \text{SFR}_{\text{UV}} + \text{SFR}_{\text{IR}, 2\sigma}$. The error bar along the y-axis considers the case of a higher dust temperature of $T_{\text{dust}} = 80$ K and the minimum SFR case of $\text{SFR}_{\text{tot}} = \text{SFR}_{\text{UV}}$. The red filled triangle and diamond are also our ALMA results for the other luminous LBGs at $z = 6$, J1211–0118 and J0217–0208, respectively, which show no significant CO(6–5) detection. The red arrows correspond to the 3σ limits. We also present the results for our $z = 6$ luminous LBGs adopting the CO SLED and α_{CO} for Althaea for their total gas mass estimates, and the previously obtained [C II] sizes as their gas sizes (red open circle: J0235–0532; red open triangle: J1211–0118; red open diamond: J0217–0208; for details, see Section 5.4). The blue squares represent the results of LBG-1 and HZ10 from left to right (Pavesi et al. 2019). Note that the data point of HZ10 is shifted by +0.1 dex along the x-axis for visibility. The blue arrow represents the 3σ limit. The orange squares are the results of AzTEC-3 and CRLE from left to right (Riechers et al. 2010, 2014; Pavesi et al. 2018; see also Pavesi et al. 2019). The brown star denotes the average of the four data points of J0235–0532, HZ10, AzTEC-3, and CRLE as the average KS relation at $z = 5$ –6, although the number of high- z sources whose Σ_{SFR} and Σ_{gas} are estimated is limited. The black open triangles and squares denote local spiral galaxies and starbursts compiled by de los Reyes & Kennicutt (2019) and Kennicutt & De Los Reyes (2021), respectively. The blue solid line corresponds to the KS relation, $\log \Sigma_{\text{SFR}} = (1.50 \pm 0.02) \log \Sigma_{\text{gas}} - 3.87 \pm 0.04$ (Kennicutt & De Los Reyes 2021) and the blue shaded region represents the Σ_{SFR} values that can be obtained when the two parameters of the KS relation change within the 2σ uncertainties. Note that the Σ_{SFR} values in de los Reyes & Kennicutt (2019) and Kennicutt & De Los Reyes (2021) are corrected by a factor of α_{KC} (Section 1) to consider the IMF difference (Table E1).

Tacconi et al. (2013) have reported that molecular gas and UV/optical light distributions of $z \sim 1$ –2 SFGs show comparable sizes, in agreement with similar findings in $z \sim 0$ SFGs (e.g., Regan et al. 2001; Leroy et al. 2008). With the r_e values obtained above, we define the gas surface density, Σ_{gas} , in a similar way to Σ_{SFR} (Equation (A7)).³⁸ The obtained Σ_{gas} values are also presented in Table 3.

Figure 9 plots Σ_{SFR} of our $z = 6$ luminous LBGs as a function of Σ_{gas} . For comparison, we also present normal spiral (disk) galaxies and starbursts in the local universe with the best-fit relation between their Σ_{SFR} and Σ_{gas} (the KS relation; de los Reyes & Kennicutt 2019; Kennicutt & De Los

³⁸ Note that our assumption that these sizes are comparable may cause a systematic uncertainty, because some previous results indicate that the sizes of CO-emitting regions are not comparable to those in the rest UV/optical, as described in the last paragraph of this section and discussed more quantitatively in Section 5.4.

Reyes 2021; see also Kennicutt 1998a),³⁹ as well as the $z = 5.3$ –5.7 sources, HZ10, LBG-1, AzTEC-3, and CRLE (Riechers et al. 2010, 2014; Pavesi et al. 2018; see also Pavesi et al. 2019). We find that J0235–0532 and HZ10 are almost at the same position in this plane, located below the local KS relation, suggesting that J0235–0532 and HZ10 have very high gas surface densities with relatively low star formation efficiencies. We also find that J1211–0118 and J0217–0208 are consistent with the local KS relation, although their obtained Σ_{gas} values are upper limits. Note that in Figure 8 their data points are consistent with the integrated KS relation, while in Figure 9 they are below the local KS relation. The reason for this is that our $z = 6$ luminous LBGs have smaller gas-emitting regions and/or larger star-forming regions than those of local starbursts. In Figure 9, we confirm that the dusty starbursts at comparable redshifts, AzTEC-3 and CRLE, are located above the local KS relation. These results may indicate that the scatter of the KS relation is larger with increasing redshift, at least at large Σ_{gas} of $\sim 10^4 M_{\odot} \text{pc}^{-2}$, possibly suggesting that star formation in high- z galaxies with high Σ_{gas} is diverse, ranging from bursty to slow. However, the number of high- z data points is still limited; this needs to be examined by investigating more objects at high redshifts in the future. Averaging the four data points for the $z = 5$ –6 galaxies of J0235–0532, HZ10, AzTEC-3, and CRLE, we find that the $z = 5$ –6 KS relation at $\Sigma_{\text{gas}} \sim 10^4 M_{\odot} \text{pc}^{-2}$ on average is consistent with the KS relation in the local universe. Again, the number of high- z sources whose Σ_{SFR} and Σ_{gas} are estimated is limited yet. It would be interesting to compare the observational results for a larger sample of high- z galaxies with those of theoretical studies in the future (e.g., Ferrara et al. 2019; Dubois et al. 2021).

Note that the r_e values measured in the rest UV continuum images are used in the calculations of both the SFR and gas surface densities for our $z = 6$ luminous LBGs. If their CO sizes are significantly larger than the rest UV sizes, the currently presented Σ_{gas} values correspond to the upper limits (e.g., Kaasinen et al. 2020). More quantitative discussion about this point is presented in Section 5.4. In order to obtain more accurate Σ_{gas} values with no such systematic uncertainties, high-resolution deep CO observations are necessary.

5.4. Systematic Uncertainties

In Sections 5.2 and 5.3, we obtain the total gas mass estimates for our $z = 6$ luminous LBGs based on our CO(6–5) observation results by carefully considering the uncertainties suggested from the previous observation results, and discuss the KS relation. However, we caution that the gas mass estimates have substantial systematic uncertainties.

One is the CO SLED uncertainty. In our discussion above, we adopt the previously observed CO SLED results for $z \sim 1$ –2 SFGs and consider the significant amount of scatter seen in observations of individual objects (Daddi et al. 2015). However, our $z = 6$ luminous LBGs may be experiencing more bursty star formation with higher gas density and thus the CO SLED could be more excited. For example, previous CO observations of nearby starbursts have revealed that their integrated CO flux ratios are about $I_{\text{CO}(6-5)}/I_{\text{CO}(1-0)} \simeq 8$ –20

³⁹ Because the Kroupa IMF is adopted in de los Reyes & Kennicutt (2019) and Kennicutt & De Los Reyes (2021) as listed in Table E1, their Σ_{SFR} values are corrected by a factor of α_{KC} (Section 1).

(Figure 1 of Mashian et al. 2015).⁴⁰ Based on the ALMA Spectroscopic Survey in the Hubble Ultra Deep Field (ASPECS), Boogaard et al. (2020) have shown that SFGs at $\langle z \rangle = 2.5$ have higher CO excitation than those at $\langle z \rangle = 1.2$ as well as the results of Daddi et al. (2015), suggesting the increased CO excitation at higher redshifts (e.g., Figure 7 of Boogaard et al. 2020). Theoretically, Vallini et al. (2018) have developed a semianalytical model for GMCs where the CO lines are excited, and postprocessed a state-of-the-art zoom-in cosmological simulation of a main-sequence galaxy at $z = 6$, Althaea, with $M_{\text{star}} \approx 10^{10} M_{\odot}$ and $\text{SFR} \approx 100 M_{\odot} \text{ yr}^{-1}$ (Pallottini et al. 2017), which is in line with the nature of the galaxies discussed in this paper, showing that the CO SLED of Althaea has a peak at around the upper-state rotational quantum number of $J_{\text{up}} \simeq 6$. Specifically, Althaea has CO luminosities of about $L'_{\text{CO}(1-0)} \simeq 10^{9.2} \text{ K km s}^{-1} \text{ pc}^2$ and $L'_{\text{CO}(6-5)} \simeq 10^{8.9} \text{ K km s}^{-1} \text{ pc}^2$, yielding the CO luminosity ratio of $L'_{\text{CO}(1-0)}/L'_{\text{CO}(6-5)} \simeq 2.0$. In contrast, the CO luminosity ratio that we have adopted in our discussion above is $L'_{\text{CO}(1-0)}/L'_{\text{CO}(6-5)} = 6.2 \pm 3.5$ (Equation (6) in Section 5.2). Although their theoretical result is just for one $z = 6$ galaxy, their upcoming results with the SERRA simulation show that the physical mechanisms exciting the CO SLED (i.e., high density and high turbulence) are common in more than 100 high- z galaxies (A. Pallottini 2022, in preparation; see also Pallottini et al. 2019). If the CO SLEDs of our $z = 6$ luminous LBGs are similar to that of Althaea, the gas mass estimates become lower by a factor of about 1/3. This should be examined by observing several CO emission lines with different excited states from high- z SFGs.

Another systematic uncertainty comes from the CO-to-H₂ conversion factor, α_{CO} . In our discussion above, we adopt the fixed value of $\alpha_{\text{CO}} = 4.5 M_{\odot} (\text{K km s}^{-1} \text{ pc}^2)^{-1}$, which is consistent with the previous observational results such as for the Milky Way, $z \sim 1-2$ SFGs, and HZ10 at $z = 5.7$ (Daddi et al. 2010; Bolatto et al. 2013; Carilli & Walter 2013; Pavesi et al. 2019). However, it is known that the CO-to-H₂ conversion factor becomes smaller in galaxies with more active star formation. In fact, LIRGs and ULIRGs show low CO-to-H₂ conversion factors of $\alpha_{\text{CO}} \simeq 0.8 M_{\odot} (\text{K km s}^{-1} \text{ pc}^2)^{-1}$ (Downes & Solomon 1998), which is often adopted in previous studies of high- z dusty starbursts (e.g., Greve et al. 2005; Riechers et al. 2010; Aravena et al. 2016; see also Wagg et al. 2009). Our $z = 6$ luminous LBGs may also have small α_{CO} values compared to the adopted one. From a theoretical point of view, Vallini et al. (2018) have shown that the simulated $z = 6$ galaxy Althaea has a small α_{CO} value of $\alpha_{\text{CO}} = 1.5 M_{\odot} (\text{K km s}^{-1} \text{ pc}^2)^{-1}$ (see their Figure 12; see also Narayanan et al. 2012). If our $z = 6$ luminous LBGs have small α_{CO} values comparable to Althaea, the gas mass estimates based on the CO(6–5) results are further reduced by a factor of 1/3. Interestingly, if we adopt the CO SLED and α_{CO} for Althaea, the obtained gas mass estimate for J0235–0532 from CO(6–5) is consistent with that obtained from the [C II] luminosity (Section 5.2).

⁴⁰ In their paper, the CO fluxes, f_{CO} , have units of W m^{-2} ; for comparison we use the following conversion obtained from Equation (A3):

$$\frac{L_{\text{CO}(6-5)}}{L_{\text{CO}(1-0)}} = \frac{f_{\text{CO}(6-5)}}{f_{\text{CO}(1-0)}} \cdot \left(\frac{\nu_{\text{CO}(6-5)}^{(\text{rest})}}{\nu_{\text{CO}(1-0)}^{(\text{rest})}} \right)^{-1}. \quad (8)$$

Here we do not consider the AGNs and Seyfert galaxies presented in their figure.

Furthermore, in the calculations of the gas surface densities of our $z = 6$ luminous LBGs, we assume that the sizes of CO-emitting regions are comparable to those of star-forming regions, which is also a source of systematic uncertainties. As mentioned in Section 5.3, some previous observational studies for $z \sim 0-2$ SFGs have shown that this is the case (Regan et al. 2001; Leroy et al. 2008; Tacconi et al. 2013), while some other studies have shown that the gas sizes are larger. For our $z = 6$ luminous LBGs, Carniani et al. (2020) have reported their [C II] sizes (FWHMs along the major axis) in their Table A1. If the [C II] sizes are comparable to those of CO-emitting regions and the CO luminosities are comparable to the current measurements, the gas sizes become larger by about a factor of 3, and thus Σ_{gas} becomes smaller by about a factor of 1/10. This can be tested by deep observations of low- J CO emission, which better traces the molecular gas distribution and the total gas mass.

If we adopt the CO SLED and α_{CO} for Althaea for total gas mass estimates, and use the previously obtained [C II] sizes as their gas sizes, then the estimated gas surface densities of our $z = 6$ luminous LBGs become smaller by about two orders of magnitude than presented in Figure 9. Figure 9 adds this possibility on the $\Sigma_{\text{SFR}}-\Sigma_{\text{gas}}$ plot. In this case, our $z = 6$ luminous LBGs are located above the KS relation, which means that they are experiencing bursty star formation. Because their [O III]/[C II] ratios are relatively high compared to local galaxies with similar total SFRs (Section 5.1), this interpretation may be physically more reasonable (Vallini et al. 2021; see also Ferrara et al. 2019). This issue is expected to be clarified by future follow-up observations.

6. Summary

In this study, we have presented our ALMA observation results for the CO(6–5) and dust continuum emission from the three luminous LBGs with $-22.8 > M_{\text{UV}} > -23.3$ mag at $z_{\text{spec}} = 6.0293-6.2037$ identified in the Subaru/HSC survey. Their [O III] 88 μm and [C II] 158 μm emission lines have been detected in the previous work (Harikane et al. 2020b). Our main results are as follows.

1. Out of the three $z = 6$ luminous LBGs, we have marginal detection of the CO(6–5) emission at the $\simeq 4\sigma$ significance level at the expected frequency from the previously detected [O III] 88 μm and [C II] 158 μm lines.
2. No dust continuum emission at $\lambda_{\text{rest}} \simeq 430 \mu\text{m}$ is significantly detected for our $z = 6$ luminous LBGs. By combining the obtained upper limits with the previous results at shorter wavelengths of $\lambda_{\text{rest}} \simeq 90-160 \mu\text{m}$, we have updated the dust continuum SED fitting analyses, and confirmed that our obtained constraints on L_{IR} and T_{dust} are consistent with the previous results of Harikane et al. (2020b).
3. We have compared the CO(6–5) and IR luminosities of our $z = 6$ luminous LBGs with those of other sources over a wide range of redshifts in the literature by taking into account the CMB effect and the T_{dust} uncertainty. We have found that our $z = 6$ luminous LBGs are consistent with the previous results owing to the relatively large uncertainties.
4. By comparing the $L_{\text{CO}}/L_{[\text{C II}]}$ and $L_{[\text{C II}]} / L_{\text{IR}}$ ratios of our $z = 6$ luminous LBGs with previous observations and results of the PDR model calculation, we have found that

J0235–0532 has a relatively high n_{H} value comparable to those of low- z LIRGs and ULIRGs, as well as those of quasars and Galactic star-forming regions with high n_{H} and U_{UV} values. We have also found that J1211–0118 and J0217–0208 have lower n_{H} values consistent with local SFGs and Galactic star-forming regions with relatively low n_{H} values.

5. By carefully taking into account the systematic uncertainties in the CO SLED, M_{gas} constraints for our $z = 6$ luminous LBGs have been obtained based on our CO(6–5) observation results. We have found that J0235–0532 is in broad agreement with SFGs at various redshifts with similar M_{gas} in the literature, including the $z = 5.3$ – 5.7 SFGs of HZ10 and LBG-1. We have also found that the M_{gas} upper limits for J1211–0118 and J0217–0208 are consistent with the previous results with comparable SFRs.
6. We have calculated the global SFR and gas surface densities of our $z = 6$ luminous LBGs based on the total SFR and M_{gas} constraints, with the sizes of star-forming regions measured in the HSC images capturing the rest UV continuum emission. We have found that J0235–0532 is at almost the same position as HZ10 on the Σ_{SFR} – Σ_{gas} plane, located slightly below the local KS relation, indicating that J0235–0532 and HZ10 have high gas surface densities with relatively low star formation efficiencies. We have also found that the upper limits of Σ_{gas} for J1211–0118 and J0217–0208 are consistent with the local KS relation. Because the dusty starbursts at similar redshifts, AzTEC-3 and CRLE, are located above the local KS relation, our results and the previous results may suggest that the scatter of the KS relation increases with increasing redshift at least at large Σ_{gas} . In addition, the average $z = 5$ – 6 KS relation at $\Sigma_{\text{gas}} \sim 10^4 M_{\odot} \text{pc}^{-2}$ is in agreement with the local KS relation. However, the number of high- z sources whose Σ_{SFR} and Σ_{gas} have been estimated is still limited; the high- z KS relation needs to be determined with better accuracy to discuss the average and the scatter by investigating more objects at high redshifts in the future.
7. We caution that the obtained gas mass estimates for our $z = 6$ luminous LBGs have substantial systematic uncertainties such as the CO SLED, the CO-to- H_2 conversion factor α_{CO} , and gas sizes. If we adopt the CO SLED and the α_{CO} value suggested by the state-of-the-art zoom-in cosmological simulation and the gas sizes measured with [C II] emission, the gas surface densities estimated for our $z = 6$ luminous LBGs can become larger by about two orders of magnitude, which opens up two conflicting possibilities regarding their location below or above the KS relation. This situation should be clarified by pursuing further CO observations of high- z SFGs.

We acknowledge the constructive comments and helpful suggestions from the anonymous referee that helped us to improve the manuscript. We appreciate the support of the staff at the ALMA Regional Center, especially Kazuya Saigo, for giving us helpful advice on analyzing the ALMA data. We are grateful to the staff of the IRAM facilities, especially Michael Bremer and Melanie Krips, for helping us to reduce the NOEMA data. We also thank Daizhong Liu for sharing their

data with us, and Marc Pound and Mark Wolfire for their helpful advice on using the results of the PDRT calculation.

This paper made use of the following ALMA data: ADS/JAO.ALMA#2019.1.00156.S and ADS/JAO.ALMA#2017.1.00508.S. ALMA is a partnership of ESO (representing its member states), NSF (USA) and NINS (Japan), together with NRC (Canada), MOST and ASIAA (Taiwan), and KASI (Republic of Korea), in cooperation with the Republic of Chile. The Joint ALMA Observatory is operated by ESO, AUI/NRAO and NAOJ.

This work is based on observations carried out under project numbers W18FB and S19DK with the IRAM NOEMA Interferometer. IRAM is supported by INSU/CNRS (France), MPG (Germany) and IGN (Spain).

The Hyper Suprime-Cam (HSC) collaboration includes the astronomical communities of Japan and Taiwan, and Princeton University. The HSC instrumentation and software were developed by the National Astronomical Observatory of Japan (NAOJ), the Kavli Institute for the Physics and Mathematics of the Universe (Kavli IPMU), the University of Tokyo, the High Energy Accelerator Research Organization (KEK), the Academia Sinica Institute for Astronomy and Astrophysics in Taiwan (ASIAA), and Princeton University. Funding was contributed by the FIRST program from the Japanese Cabinet Office, the Ministry of Education, Culture, Sports, Science and Technology (MEXT), the Japan Society for the Promotion of Science (JSPS), Japan Science and Technology Agency (JST), the Toray Science Foundation, NAOJ, Kavli IPMU, KEK, ASIAA, and Princeton University.

This paper makes use of software developed for the Large Synoptic Survey Telescope. We thank the LSST Project for making their code available as free software at <http://dm.lsst.org>.

This paper is based in part on data collected at the Subaru Telescope and retrieved from the HSC data archive system, which is operated by Subaru Telescope and Astronomy Data Center (ADC) at NAOJ. Data analysis was in part carried out with the cooperation of Center for Computational Astrophysics (CfCA), NAOJ.

The Pan-STARRS1 Surveys (PS1) and the PS1 public science archive have been made possible through contributions by the Institute for Astronomy, the University of Hawaii, the Pan-STARRS Project Office, the Max Planck Society and its participating institutes, the Max Planck Institute for Astronomy, Heidelberg, and the Max Planck Institute for Extraterrestrial Physics, Garching, The Johns Hopkins University, Durham University, the University of Edinburgh, the Queen's University Belfast, the Harvard-Smithsonian Center for Astrophysics, the Las Cumbres Observatory Global Telescope Network Incorporated, the National Central University of Taiwan, the Space Telescope Science Institute, the National Aeronautics and Space Administration under grant No. NNX08AR22G issued through the Planetary Science Division of the NASA Science Mission Directorate, the National Science Foundation grant No. AST-1238877, the University of Maryland, Eotvos Lorand University (ELTE), the Los Alamos National Laboratory, and the Gordon and Betty Moore Foundation.

This work has made use of data from the European Space Agency (ESA) mission Gaia (<https://www.cosmos.esa.int/gaia>), processed by the Gaia Data Processing and Analysis Consortium (DPAC, <https://www.cosmos.esa.int/web/gaia/>)

dpac/consortium). Funding for the DPAC has been provided by national institutions, in particular the institutions participating in the Gaia Multilateral Agreement.

This work was partially performed using the computer facilities of the Institute for Cosmic Ray Research, The University of Tokyo. This work was supported by the World Premier International Research Center Initiative (WPI Initiative), MEXT, Japan, as well as KAKENHI grant Nos. 15K17602, 15H02064, 17H01110, 17H01114, 19K14752, 20H00180, and 21H04467 through the Japan Society for the Promotion of Science (JSPS). This work was partially supported by the joint research program of the Institute for Cosmic Ray Research (ICRR), University of Tokyo. A.F., A. P., and L.V. acknowledge support from the ERC Advanced Grant INTERSTELLAR H2020/740120. A.F. acknowledges generous support from the Carl Friedrich von Siemens-Forschungspreis der Alexander von Humboldt-Stiftung Research Award. A.K.I. and Y.S. are supported by NAOJ ALMA Scientific Research Grant Code 2020-16B. T.H. was supported by Leading Initiative for Excellent Young Researchers, MEXT, Japan (HJH02007) and KAKENHI (20K22358).

Software: IRAF (Tody 1986, 1993),⁴¹ SAOImage DS9 (Joye & Mandel 2003), Numpy (Harris et al. 2020), Matplotlib (Hunter 2007), Scipy (Virtanen et al. 2020), Astropy (Astropy Collaboration et al. 2013, 2018),⁴² and Ned Wright’s Javascript Cosmology Calculator (Wright 2006),⁴³ CASA (McMullin et al. 2007), GILDAS (Guiloteau & Lucas 2000; Pety 2005; Gildas Team 2013), SExtractor (Bertin & Arnouts 1996), GALFIT (Peng et al. 2002, 2010).

Appendix A Standard Equations

In this appendix, we present the standard equations used in this study for reference.

In Section 2, we estimate SFRs for our $z = 6$ luminous LBGs by using Equation (1) of Kennicutt (1998b),

$$\text{SFR}_{\text{UV}} = 1.4 \times 10^{-28} \alpha_{\text{SC}} L_{\nu}, \quad (\text{A1})$$

where L_{ν} is the rest UV luminosity density in units of $\text{erg s}^{-1} \text{Hz}^{-1}$, and Equation (4) of Kennicutt (1998b),⁴⁴

$$\text{SFR}_{\text{IR}} = 4.5 \times 10^{-44} \alpha_{\text{SC}} L_{\text{IR}}, \quad (\text{A2})$$

where L_{IR} is the IR luminosity integrated over the wavelength range 8–1000 μm in units of erg s^{-1} . We multiply by α_{SC} to convert from the Salpeter IMF to the Chabrier IMF.

In Section 4.1, from the integrated CO(6–5) emission line flux, we obtain the CO(6–5) luminosity in units of L_{\odot} by using Equation (18) of Casey et al. (2014),

$$L_{\text{CO}} = 1.04 \times 10^{-3} I_{\text{CO}} \frac{\nu_{\text{CO}}^{(\text{rest})}}{1+z} D_{\text{L}}^2(z), \quad (\text{A3})$$

⁴¹ IRAF is distributed by the National Optical Astronomy Observatory, which is operated by the Association of Universities for Research in Astronomy (AURA) under a cooperative agreement with the National Science Foundation.

⁴² <http://www.astropy.org>

⁴³ <http://www.astro.ucla.edu/~wright/CosmoCalc.html>

⁴⁴ Note that this conversion does not take into account the contribution from old stars whose emission is absorbed by dust and reradiated in the IR spectral range, although it would not be significant for high- z LBGs. In order to estimate SFRs from IR continuum luminosities by appropriately considering the contribution from old stars, one needs a more general recipe such as the one derived by Inoue et al. (2000; see also Hirashita et al. 2003).

where I_{CO} is the integrated CO flux in units of Jy km s^{-1} and $D_{\text{L}}(z)$ is the luminosity distance in Mpc. We also calculate the CO(6–5) luminosity in units of $\text{K km s}^{-1} \text{pc}^2$ defined as Equation (19) of Casey et al. (2014),

$$L'_{\text{CO}} = 3.25 \times 10^7 I_{\text{CO}} \frac{D_{\text{L}}^2(z)}{(1+z)^3 \nu_{\text{CO}}^{(\text{obs})2}}, \quad (\text{A4})$$

where $\nu_{\text{CO}}^{(\text{obs})} = \nu_{\text{CO}}^{(\text{rest})}/(1+z)$.

In Section 4.2, the intrinsic dust continuum flux densities of a modified blackbody SED at a given observed frequency ν_{obs} are calculated from (e.g., Ouchi et al. 1999; Ono et al. 2014)

$$f_{\nu}^{(\text{int})} = \frac{(1+z)L_{\text{IR}}}{4\pi D_{\text{L}}^2(z)} \frac{\nu_0^{\beta_{\text{d}}} B(\nu_0, T_{\text{dust}})}{\int \nu^{\beta_{\text{d}}} B(\nu, T_{\text{dust}}) d\nu}, \quad (\text{A5})$$

where $B(\nu, T)$ is the Planck function and $\nu_0 = \nu_{\text{obs}}(1+z)$. We assume a spectral index of $\beta_{\text{d}} = 1.5$, which is consistent with local measurements for SFGs (e.g., Dunne & Eales 2001; Gordon et al. 2010; Casey 2012) and often adopted in previous high- z studies (e.g., Casey et al. 2014; Franco et al. 2020; Harikane et al. 2020b; see also Sugahara et al. 2021; Schouws et al. 2022). Harikane et al. (2020b) have confirmed that this assumption does not significantly affect the fitting results of the other parameters for our targets.

In Section 5.3, we define SFR surface density, Σ_{SFR} , in units of $M_{\odot} \text{yr}^{-1} \text{kpc}^{-2}$ as the average SFR in a circular region whose half-light radius is r_{e} ,

$$\Sigma_{\text{SFR}} = \frac{\text{SFR}}{2\pi r_{\text{e}}^2}. \quad (\text{A6})$$

The multiplicative factor of 1/2 is applied because the SFR is estimated from the total luminosity while the area is calculated with the half-light radius (e.g., Hathi et al. 2008; Tacconi et al. 2013; Decarli et al. 2016). In a similar way, we define the gas surface density as

$$\Sigma_{\text{gas}} = \frac{M_{\text{gas}}}{2\pi r_{\text{e}}^2}. \quad (\text{A7})$$

Appendix B NOEMA Observations

In addition to the ALMA observations described in Section 3, two of our targets, J1211–0118 and J0217–0208, were also observed with NOEMA using 9–10 antennas between 2019 January 20 and 2019 August 15 (Proposal IDs: W18FB and S19DK; PI: Y. Ono). The antenna configurations were A and D, i.e., the most extended and the compact configurations, respectively. We used the NOEMA receiver 1 to observe the CO(6–5) emission as well as the dust continuum emission from the two LBGs. The total observing times were 5.5 hr for J1211–0118 and 13.9 hr for J0217–0208. All the NOEMA data are reduced using the GILDAS software.⁴⁵ The 1σ flux density levels for the continuum images are $13.8 \mu\text{Jy beam}^{-1}$ for J1211–0118 and $13.9 \mu\text{Jy beam}^{-1}$ for J0217–0208. The NOEMA data show no significant detection of either dust continuum emission or CO emission, which is consistent with the ALMA results (Section 4.2).

⁴⁵ <https://www.iram.fr/IRAMFR/GILDAS/>

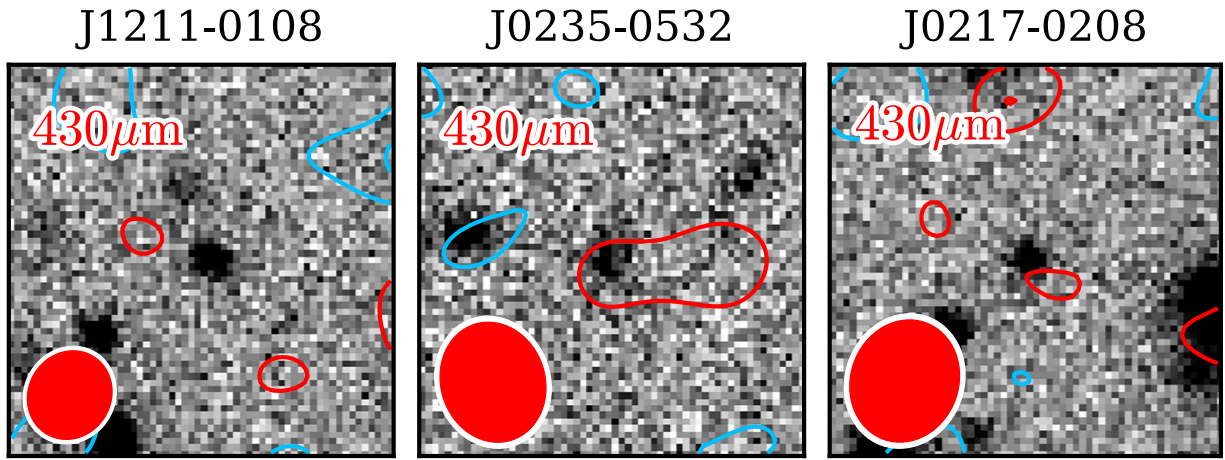


Figure 10. Dust continuum emission maps for our $z = 6$ luminous LBGs, J1211–0118, J0235–0532, and J0217–0208 from left to right. The red contours are continuum emission at $\lambda_{\text{rest}} \simeq 430 \mu\text{m}$ drawn at 1σ intervals from 1.5σ . Although the dust continuum of J0235 and J0217 may show a $\sim 2\sigma$ signal, in this paper we conservatively use their 3σ upper limits. The blue lines represent negative contours from -1.5σ at 1σ intervals. The red ellipses at the lower left corner denote the ALMA synthesized beams. The gray backgrounds are the Subaru HSC z -band images that capture the rest UV continuum emission from our targets. The size of each image is $10'' \times 10''$.

Appendix C Dust Continuum Emission Maps

In Figure 10, we present the dust continuum emission maps at $\lambda_{\text{obs}} \simeq 3 \text{ mm}$ ($\lambda_{\text{rest}} \simeq 430 \mu\text{m}$) obtained with ALMA for our $z = 6$ luminous LBGs. For J0235–0532, the $\pm 300 \text{ km s}^{-1}$ range around the CO(6–5) line is removed.

Appendix D Extra Results Related to Gas Masses

In addition to the comparisons between gas masses and SFRs as well as the Kennicutt–Schmidt relation shown in Section 5, in this appendix we present the gas fractions and gas depletion timescales for comparisons with previous results, although the systematic uncertainties on these estimates are also not small as discussed in Section 5.4.

D.1. Gas Fraction

We constrain gas fractions for our $z = 6$ luminous LBGs. The gas fraction is defined as

$$f_{\text{gas}} = \frac{M_{\text{gas}}}{M_{\text{gas}} + M_{\text{star}}}, \quad (\text{D1})$$

where M_{star} is the stellar mass. For our $z = 6$ luminous LBGs, M_{star} can be roughly estimated from M_{UV} by using the relation between M_{star} and M_{UV} for SFGs at similar redshifts, e.g., Equation (2) of Shibuya et al. (2015),

$$\log M_{\text{star}} = -2.45 - 0.59M_{\text{UV}} + \log \beta_{\text{SC}}, \quad (\text{D2})$$

where $\beta_{\text{SC}} = 1/1.64 \simeq 0.61$ is the factor to convert from M_{star} with the Salpeter (1955) IMF to that with the Chabrier (2003) IMF (Madau & Dickinson 2014; see also Table E1). We present the obtained f_{gas} constraints in Table 3. Note that our f_{gas} constraints do not include the systematic uncertainty in the stellar mass estimates from the UV luminosity, which is about ± 0.5 dex due to differences in stellar population properties such as star formation history (Shibuya et al. 2015). For more robust discussion, deep rest-frame optical data that can probe the stellar continuum emission are required.

Table E1
IMFs Adopted in the Previous Studies

Previous Study	IMF
Riechers et al. (2014)	Chabrier (2003)
Béthermin et al. (2015)	Chabrier (2003)
Shibuya et al. (2015)	Salpeter (1955)
Scoville et al. (2016)	Chabrier (2003)
Aravena et al. (2016)	Chabrier (2003)
Schinnerer et al. (2016)	Chabrier (2003)
Magdis et al. (2017)	Chabrier (2003)
Saintonge et al. (2017)	Chabrier (2003)
Pavesi et al. (2018)	Chabrier (2003)
de los Reyes & Kennicutt (2019)	Kroupa (2001)
Pavesi et al. (2019)	Chabrier (2003)
Harikane et al. (2020b)	Chabrier (2003)
Dessauges-Zavadsky et al. (2020)	Chabrier (2003)
Kennicutt & De Los Reyes (2021)	Kroupa (2001)

In Figure 11, we present f_{gas} of our $z = 6$ luminous LBGs with those of lower- z SFGs (Béthermin et al. 2015; Scoville et al. 2016; Saintonge et al. 2017) as well as the $z = 5.3$ – 5.7 sources, HZ10, LBG-1, AzTEC-3, and CRLE (Riechers et al. 2010, 2014; Pavesi et al. 2018; see also Pavesi et al. 2019) as a function of total SFR. We find that J0235–0532 has a comparable gas fraction to lower- z SFGs with similar SFRs. We also find that the obtained upper limits on the gas fractions of J1211–0118 and J0217–0208 are consistent with lower- z SFGs with similar SFRs. Compared to HZ10, the gas fraction of J0235–0532 is consistent owing to the large uncertainties, while those of J1211–0118 and J0217–0208 are significantly lower, although their total SFRs are comparable.

D.2. Evolution of the Gas Depletion Timescale

Figure 12 shows the gas depletion timescale, $t_{\text{dep}} = M_{\text{gas}}/\text{SFR}$, as a function of redshift. For comparison, we also present the results for the four $z = 5.3$ – 5.7 sources of HZ10, LBG-1, AzTEC-3, and CRLE (Riechers et al. 2010, 2014; Pavesi et al. 2018; see also Pavesi et al. 2019), the average results for $z = 4.4$ – 5.9 LBGs with $M_{\text{star}} = 10^{8.4-11} M_{\odot}$ obtained in the ALMA Large Program to

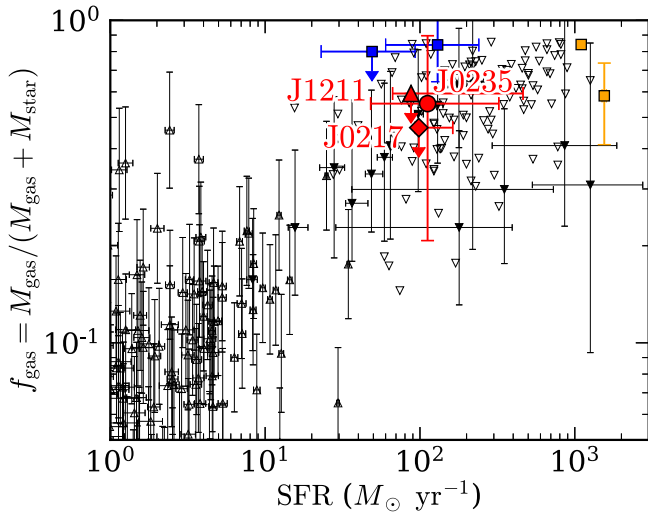


Figure 11. Gas fraction, $f_{\text{gas}} = M_{\text{gas}} / (M_{\text{gas}} + M_{\text{star}})$, as a function of SFR. The red circle is our ALMA result for a luminous LBG at $z = 6$ with $\simeq 4\sigma$ CO(6–5) detection, J0235–0532, in the case of $T_{\text{dust}} = 50$ K and $\text{SFR}_{\text{tot}} = \text{SFR}_{\text{UV}} + \text{SFR}_{\text{IR},2\sigma}$. The error bar along the y-axis considers the case of a higher dust temperature of $T_{\text{dust}} = 80$ K and the minimum SFR case of $\text{SFR}_{\text{tot}} = \text{SFR}_{\text{UV}}$. The red triangle and diamond are also our ALMA results for the other luminous LBGs at $z = 6$, J1211–0118 and J0217–0208, respectively, which show no significant CO(6–5) detection. The red arrows correspond to the 3σ limits. The blue squares represent the results of LBG-1 and HZ10 from left to right (Pavesi et al. 2019). The blue arrow represents the 3σ limit. The orange squares are the results of AzTEC-3 and CRLE from left to right (Riechers et al. 2010, 2014; Pavesi et al. 2018; see also Pavesi et al. 2019). The black filled downward triangles are the results of SFGs with $M_{\text{star}} > 3 \times 10^{10} M_{\odot}$ at $z \sim 0$ –4 using stacked dust SEDs (B  thermin et al. 2015). The black open downward triangles show the results of SFGs with $M_{\text{star}} > 2 \times 10^{10} M_{\odot}$ at $z \sim 1$ –6 based on submillimeter dust continuum measurements (Scoville et al. 2016). The black open triangles are the results for low- z galaxies at $z = 0.01$ –0.05 (Saintonge et al. 2017).

Investigate [C II] at Early Times (ALPINE; Dessauges-Zavadsky et al. 2020), and other SFGs including dusty starbursts over a wide range of redshifts (B  thermin et al. 2015; Aravena et al. 2016; Schinnerer et al. 2016; Scoville et al. 2016; Magdis et al. 2017; Saintonge et al. 2017).

As expected from Figure 8, t_{dep} of J0235–0532 is comparable to those of lower- z SFGs at $z \sim 2$ –3. Based on previous results for lower- z SFGs, Tacconi et al. (2013) have suggested a redshift dependence of the gas depletion timescale in the form of $t_{\text{dep}} \propto (1+z)^{-1.0}$, which is shallower than what is expected if t_{dep} is proportional to the dynamical timescale, $t_{\text{dep}} \propto (1+z)^{-1.5}$ (Dav   et al. 2011, 2012; see also Saintonge et al. 2013). Our results for J0235–0532 show that the t_{dep} value is likely to be larger than expected from the previously reported redshift dependences. For the other two $z = 6$ luminous LBGs, J1211–0118 and J0217–0208, we have obtained upper limits on their t_{dep} , indicating that their t_{dep} values can be significantly shorter than that for J0235–0532. In other words, there is a possibility that t_{dep} values of high- z SFGs are not necessarily as large as those of lower- z SFGs, suggesting that J0235–0532 may be an outlier with large t_{dep} . Similar arguments can be made at slightly lower redshifts based on the results of HZ10 and LBG-1 as well as the ALPINE results. Because the previous results for lower- z SFGs show a large scatter of t_{dep} , it would be interesting to investigate a typical t_{dep} value by observing more high- z SFGs with better sensitivities in future studies to characterize the typical star formation properties in high- z SFGs.

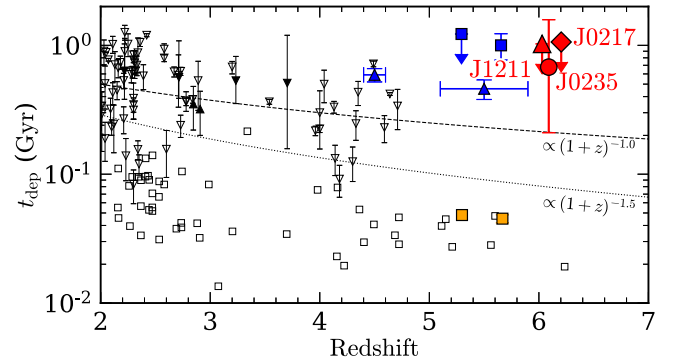








Figure 12. Redshift evolution of the gas depletion time, $t_{\text{dep}} = M_{\text{gas}} / \text{SFR}$. The red circle is our ALMA result for a luminous LBG at $z = 6$ with $\simeq 4\sigma$ CO(6–5) detection, J0235–0532, in the case of $T_{\text{dust}} = 50$ K and $\text{SFR}_{\text{tot}} = \text{SFR}_{\text{UV}} + \text{SFR}_{\text{IR},2\sigma}$. The error bar along the y-axis for J0235–0532 considers the case of a higher dust temperature of $T_{\text{dust}} = 80$ K and the minimum SFR case of $\text{SFR}_{\text{tot}} = \text{SFR}_{\text{UV}}$. The red triangle and diamond are also our ALMA results for the other luminous LBGs at $z = 6$, J1211–0118 and J0217–0208, respectively, which show no significant CO(6–5) detection. The red arrows correspond to the 3σ limits. The blue squares represent the results of LBG-1 and HZ10 from left to right (Pavesi et al. 2019). The blue arrow represents the 3σ limit. The orange squares are the results of AzTEC-3 and CRLE from left to right (Riechers et al. 2010, 2014; Pavesi et al. 2018; see also Pavesi et al. 2019). The blue filled triangles show the average results of $z = 4.4$ –5.9 LBGs with $M_{\text{star}} = 10^{8.4-11} M_{\odot}$ obtained in the ALPINE survey (Dessauges-Zavadsky et al. 2020), where M_{gas} are estimated from the [C II] luminosities. The black filled triangles denote the results based on CO observations of $z \sim 3$ LBGs (Magdis et al. 2017). The black filled downward triangles are the results of SFGs with $M_{\text{star}} > 3 \times 10^{10} M_{\odot}$ using stacked dust SEDs (B  thermin et al. 2015). The black open downward triangles show the results of SFGs with $M_{\text{star}} > 2 \times 10^{10} M_{\odot}$ based on submillimeter dust continuum measurements (Schinnerer et al. 2016; Scoville et al. 2016). The black open squares are the results for lensed/unlensed dusty starburst sources compiled by Aravena et al. (2016). The dashed and dotted lines correspond to the curves of $t_{\text{dep}} \propto (1+z)^{-1.0}$ and $t_{\text{dep}} \propto (1+z)^{-1.5}$ (e.g., Dav   et al. 2012; Tacconi et al. 2013), which are normalized to the typical gas depletion time of 1.5 Gyr observed for local galaxies (Leroy et al. 2008; Bigiel et al. 2011; Saintonge et al. 2011, 2012; see also Saintonge et al. 2013).

Appendix E Adopted IMFs in the Literature

In this paper, we have adopted the Chabrier (2003) IMF with lower and upper mass cutoffs of $0.1 M_{\odot}$ and $100 M_{\odot}$, respectively, as described in Section 1. However, some previous studies have adopted different IMFs, and corrections for IMF differences are required when comparing physical quantities related to IMFs such as SFR and M_{star} . For convenience in such purposes, Table E1 summarizes the IMFs adopted in the previous studies whose SFR or M_{star} estimates are used for comparisons with our results. Where necessary to convert SFR and M_{star} values in the literature, we use constant factors of α_{SC} , α_{KC} , and β_{SC} , as described in Section 1 and Appendix D.1.

ORCID iDs

Yoshiaki Ono <https://orcid.org/0000-0001-9011-7605>
 Seiji Fujimoto <https://orcid.org/0000-0001-7201-5066>
 Yuichi Harikane <https://orcid.org/0000-0002-6047-430X>
 Masami Ouchi <https://orcid.org/0000-0002-1049-6658>
 Livia Vallini <https://orcid.org/0000-0002-3258-3672>
 Andrea Ferrara <https://orcid.org/0000-0002-9400-7312>
 Andrea Pallottini <https://orcid.org/0000-0002-7129-5761>
 Akio K. Inoue <https://orcid.org/0000-0002-7779-8677>
 Masatoshi Imanishi <https://orcid.org/0000-0001-6186-8792>

Kazuhiro Shimasaku  <https://orcid.org/0000-0002-2597-2231>
 Takuya Hashimoto  <https://orcid.org/0000-0002-0898-4038>
 Chien-Hsiu Lee  <https://orcid.org/0000-0003-1700-5740>
 Yuma Sugahara  <https://orcid.org/0000-0001-6958-7856>
 Yoichi Tamura  <https://orcid.org/0000-0003-4807-8117>
 Kotaro Kohno  <https://orcid.org/0000-0002-4052-2394>
 Malte Schramm  <https://orcid.org/0000-0001-7825-0075>

References

- Aihara, H., Arimoto, N., Armstrong, R., et al. 2018, *PASJ*, 70, S4
 Aihara, H., ALSayyad, Y., Ando, M., et al. 2019, *PASJ*, 71, 114
 Apostolovski, Y., Aravena, M., Anguita, T., et al. 2019, *A&A*, 628, A23
 Arata, S., Yajima, H., Nagamine, K., Li, Y., & Khochfar, S. 2019, *MNRAS*, 488, 2629
 Aravena, M., Spilker, J. S., Bethermin, M., et al. 2016, *MNRAS*, 457, 4406
 Astropy Collaboration, Price-Whelan, A. M., Sipőcz, B. M., et al. 2018, *AJ*, 156, 123
 Astropy Collaboration, Robitaille, T. P., Tollerud, E. J., et al. 2013, *A&A*, 558, A33
 Baker, A. J., Tacconi, L. J., Genzel, R., Lehnert, M. D., & Lutz, D. 2004, *ApJ*, 604, 125
 Bakx, T. J. L. C., Tamura, Y., Hashimoto, T., et al. 2020, *MNRAS*, 493, 4294
 Behrens, C., Pallottini, A., Ferrara, A., Gallerani, S., & Vallini, L. 2018, *MNRAS*, 477, 552
 Benford, D. J., Cox, P., Omont, A., Phillips, T. G., & McMahon, R. G. 1999, *ApJL*, 518, L65
 Bertin, E., & Arnouts, S. 1996, *A&AS*, 117, 393
 Bertoldi, F., Cox, P., Neri, R., et al. 2003, *A&A*, 409, L47
 Bethermin, M., Daddi, E., Magdis, G., et al. 2015, *A&A*, 573, A113
 Bigiel, F., Leroy, A. K., Walter, F., et al. 2011, *ApJL*, 730, L13
 Bolatto, A. D., Wolfire, M., & Leroy, A. K. 2013, *ARA&A*, 51, 207
 Boogaard, L. A., Werf, P. v. d., Weiss, A., et al. 2020, *ApJ*, 902, 109
 Bothwell, M. S., Smail, I., Chapman, S. C., et al. 2013, *MNRAS*, 429, 3047
 Bowler, R. A. A., Adams, N. J., Jarvis, M. J., & Häuβler, B. 2021, *MNRAS*, 502, 662
 Capak, P. L., Carilli, C., Jones, G., et al. 2015, *Natur*, 522, 455
 Carilli, C. L., & Walter, F. 2013, *ARA&A*, 51, 105
 Carniani, S., Ferrara, A., Maiolino, R., et al. 2020, *MNRAS*, 499, 5136
 Carniani, S., Gallerani, S., Vallini, L., et al. 2019, *MNRAS*, 489, 3939
 Carniani, S., Maiolino, R., Pallottini, A., et al. 2017, *A&A*, 605, A42
 Casey, C. M. 2012, *MNRAS*, 425, 3094
 Casey, C. M., Narayanan, D., & Cooray, A. 2014, *PhR*, 541, 45
 Casey, C. M., Zavala, J. A., Aravena, M., et al. 2019, *ApJ*, 887, 55
 Chabrier, G. 2003, *PASP*, 115, 763
 Chambers, K. C., Magnier, E. A., Metcalfe, N., et al. 2016, arXiv:1612.05560
 Cormier, D., Abel, N. P., Hony, S., et al. 2019, *A&A*, 626, A23
 Croxall, K. V., Smith, J. D., Pellegrini, E., et al. 2017, *ApJ*, 845, 96
 da Cunha, E., Groves, B., Walter, F., et al. 2013, *ApJ*, 766, 13
 Dabrowski, I. 1984, *CalPh*, 62, 1639
 Daddi, E., Dannerbauer, H., Liu, D., et al. 2015, *A&A*, 577, A46
 Daddi, E., Elbaz, D., Walter, F., et al. 2010, *ApJL*, 714, L118
 Davé, R., Finlator, K., & Oppenheimer, B. D. 2011, *MNRAS*, 416, 1354
 Davé, R., Finlator, K., & Oppenheimer, B. D. 2012, *MNRAS*, 421, 98
 de los Reyes, M. A. C., & Kennicutt, R. C., Jr. 2019, *ApJ*, 872, 16
 Decarli, R., Walter, F., Aravena, M., et al. 2016, *ApJ*, 833, 70
 Decataldo, D., Ferrara, A., Pallottini, A., Gallerani, S., & Vallini, L. 2017, *MNRAS*, 471, 4476
 Dessauges-Zavadsky, M., Ginolfi, M., Pozzi, F., et al. 2020, *A&A*, 643, A5
 D'Orlando, V., Feruglio, C., Ferrara, A., et al. 2018, *ApJL*, 863, L29
 Downes, D., & Solomon, P. M. 1998, *ApJ*, 507, 615
 Draine, B. T. 2011, *Physics of the Interstellar and Intergalactic Medium* (Princeton, NJ: Princeton Univ. Press)
 Dubois, Y., Beckmann, R., Bournaud, F., et al. 2021, *A&A*, 651, A109
 Dunne, L., & Eales, S. A. 2001, *MNRAS*, 327, 697
 Ferland, G. J., Chatzikos, M., Guzmán, F., et al. 2017, *RMxAA*, 53, 385
 Ferland, G. J., Korista, K. T., Verner, D. A., et al. 1998, *PASP*, 110, 761
 Ferrara, A., Vallini, L., Pallottini, A., et al. 2019, *MNRAS*, 489, 1
 Finke, J. D., Reyes, L. C., Georganopoulos, M., et al. 2015, *ApJ*, 814, 20
 Fisher, R. A. 1970, *Statistical Methods for Research Workers* (Edinburgh: Oliver and Boyd)
 Franco, M., Elbaz, D., Zhou, L., et al. 2020, *A&A*, 643, A30
 Fujimoto, S., Ouchi, M., Ferrara, A., et al. 2019, *ApJ*, 887, 107
 Fujimoto, S., Silverman, J. D., Bethermin, M., et al. 2020, *ApJ*, 900, 1
 Gaia Collaboration, Brown, A. G. A., Vallenari, A., et al. 2021, *A&A*, 649, A1
 Gaia Collaboration, Prusti, T., de Bruijne, J. H. J., et al. 2016, *A&A*, 595, A1
 Gildas Team 2013, GILDAS: Grenoble Image and Line Data Analysis Software, Astrophysics Source Code Library, record ascl:1305.010
 Ginolfi, M., Maiolino, R., Nagao, T., et al. 2017, *MNRAS*, 468, 3468
 González-López, J., Riechers, D. A., Decarli, R., et al. 2014, *ApJ*, 784, 99
 Gordon, K. D., Galliano, F., Hony, S., et al. 2010, *A&A*, 518, L89
 Greve, T. R., Bertoldi, F., Smail, I., et al. 2005, *MNRAS*, 359, 1165
 Guilloteau, S., & Lucas, R. 2000, in ASP Conf. Ser. 217, *Imaging at Radio through Submillimeter Wavelengths*, ed. J. G. Mangum & S. J. E. Radford (San Francisco, CA: ASP), 299
 Habing, H. J. 1968, *Bull. Astron. Inst. Netherlands*, 19, 421
 Harikane, Y., Laporte, N., Ellis, R. S., & Matsuoka, Y. 2020a, *ApJ*, 902, 117
 Harikane, Y., Ouchi, M., Inoue, A. K., et al. 2020b, *ApJ*, 896, 93
 Harris, C. R., Millman, K. J., van der Walt, S. J., et al. 2020, *Natur*, 585, 357
 Hashimoto, T., Inoue, A. K., Mawatari, K., et al. 2019, *PASJ*, 71, 71
 Hashimoto, T., Inoue, A. K., Sugahara, Y., et al. 2022, arXiv:2203.01345
 Hashimoto, T., Laporte, N., Mawatari, K., et al. 2018, *Natur*, 557, 392
 Hathi, N. P., Malhotra, S., & Rhoads, J. E. 2008, *ApJ*, 673, 686
 Heard, N. A., & Rubin-Delanchy, P. 2018, *Biométrica*, 105, 239
 Herrera-Camus, R., Förster Schreiber, N., Genzel, R., et al. 2021, *A&A*, 649, A31
 Hirashita, H., Buat, V., & Inoue, A. K. 2003, *A&A*, 410, 83
 Hogg, D. W. 1999, arXiv:astro-ph/9905116
 Holwerda, B. W., Bridge, J. S., Steele, R. L., et al. 2020, *AJ*, 160, 154
 Hunter, J. D. 2007, *CSE*, 9, 90
 Inoue, A. K., Hashimoto, T., Chihara, H., & Koike, C. 2020, *MNRAS*, 495, 1577
 Inoue, A. K., Hirashita, H., & Kamaya, H. 2000, *PASJ*, 52, 539
 Inoue, A. K., Tamura, Y., Matsuo, H., et al. 2016, *Sci*, 352, 1559
 Inoue, D., Yun, M. S., Elvis, M., et al. 2006, *ApJL*, 645, L97
 Joye, W. A., & Mandel, E. 2003, in ASP Conf. Ser. 295, *Astronomical Data Analysis Software and Systems XII*, ed. H. E. Payne, R. I. Jedrzejewski, & R. N. Hook (San Francisco, CA: ASP), 489
 Kaasinen, M., Walter, F., Novak, M., et al. 2020, *ApJ*, 899, 37
 Katz, H., Kimm, T., Sijacki, D., & Haehnelt, M. G. 2017, *MNRAS*, 468, 4831
 Kaufman, M. J., Wolfire, M., & Hollenbach, D. J. 2006, *ApJ*, 644, 283
 Kaufman, M. J., Wolfire, M. G., Hollenbach, D. J., & Luhman, M. L. 1999, *ApJ*, 527, 795
 Kawamata, R., Ishigaki, M., Shimasaku, K., et al. 2018, *ApJ*, 855, 4
 Kennicutt, R. C., Jr. 1998a, *ApJ*, 498, 541
 Kennicutt, R. C., Jr. 1998b, *ARA&A*, 36, 189
 Kennicutt, R. C., Jr., & De Los Reyes, M. A. C. 2021, *ApJ*, 908, 61
 Kikuchi, Y., Harikane, Y., Ouchi, M., et al. 2022, *ApJ*, 931, 97
 Kohandel, M., Pallottini, A., Ferrara, A., et al. 2019, *MNRAS*, 487, 3007
 Kroupa, P. 2001, *MNRAS*, 322, 231
 Lagache, G., Cousin, M., & Chatzikos, M. 2018, *A&A*, 609, A130
 Laporte, N., Katz, H., Ellis, R. S., et al. 2019, *MNRAS*, 487, L81
 Leipski, C., Meisenheimer, K., Walter, F., et al. 2013, *ApJ*, 772, 103
 Leroy, A. K., Walter, F., Brinks, E., et al. 2008, *AJ*, 136, 2782
 Liu, D., Gao, Y., Isaak, K., et al. 2015, *ApJL*, 810, L14
 Madau, P., & Dickinson, M. 2014, *ARA&A*, 52, 415
 Magdis, G. E., Rigopoulou, D., Daddi, E., et al. 2017, *A&A*, 603, A93
 Maiolino, R., Cox, P., Caselli, P., et al. 2005, *A&A*, 440, L51
 Maiolino, R., Neri, R., Beelen, A., et al. 2007, *A&A*, 472, L33
 Mashian, N., Sturm, E., Sternberg, A., et al. 2015, *ApJ*, 802, 81
 Matsuoka, Y., Onoue, M., Kashikawa, N., et al. 2018, *PASJ*, 70, S35
 McKee, C. F., & Ostriker, E. C. 2007, *ARA&A*, 45, 565
 McMullin, J. P., Waters, B., Schiebel, D., Young, W., & Golap, K. 2007, in ASP Conf. Ser. 376, *Astronomical Data Analysis Software and Systems XVI*, ed. R. A. Shaw, F. Hill, & D. J. Bell (San Francisco, CA: ASP), 127
 Mosleh, M., Williams, R. J., Franx, M., et al. 2012, *ApJL*, 756, L12
 Mulders, G. D., Pascucci, I., Apai, D., & Ciesla, F. J. 2018, *AJ*, 156, 24
 Narayanan, D., Krumholz, M. R., Ostriker, E. C., & Hernquist, L. 2012, *MNRAS*, 421, 3127
 Neri, R., Genzel, R., Ivison, R. J., et al. 2003, *ApJL*, 597, L113
 Newman, A. B., Ellis, R. S., Bundy, K., & Treu, T. 2012, *ApJ*, 746, 162
 Oesch, P. A., Bouwens, R. J., Carollo, C. M., et al. 2010, *ApJL*, 709, L21
 Oke, J. B., & Gunn, J. E. 1983, *ApJ*, 266, 713
 Olsen, K., Greve, T. R., Narayanan, D., et al. 2017, *ApJ*, 846, 105
 Ono, Y., Ouchi, M., Curtis-Lake, E., et al. 2013, *ApJ*, 777, 155
 Ono, Y., Ouchi, M., Harikane, Y., et al. 2018, *PASJ*, 70, S10
 Ono, Y., Ouchi, M., Kurono, Y., & Momose, R. 2014, *ApJ*, 795, 5
 Ouchi, M., Yamada, T., Kawai, H., & Ohta, K. 1999, *ApJL*, 517, L19
 Pallottini, A., Ferrara, A., Bovino, S., et al. 2017, *MNRAS*, 471, 4128

- Pallottini, A., Ferrara, A., Decataldo, D., et al. 2019, *MNRAS*, **487**, 1689
- Pallottini, A., Gallerani, S., Ferrara, A., et al. 2015, *MNRAS*, **453**, 1898
- Pavesi, R., Riechers, D. A., Faisst, A. L., Stacey, G. J., & Capak, P. L. 2019, *ApJ*, **882**, 168
- Pavesi, R., Riechers, D. A., Sharon, C. E., et al. 2018, *ApJ*, **861**, 43
- Peng, C. Y., Ho, L. C., Impey, C. D., & Rix, H.-W. 2002, *AJ*, **124**, 266
- Peng, C. Y., Ho, L. C., Impey, C. D., & Rix, H.-W. 2010, *AJ*, **139**, 2097
- Pensabene, A., Decarli, R., Bañados, E., et al. 2021, *A&A*, **652**, A66
- Pety, J. 2005, in SF2A-2005: Semaine de l'Astrophysique Française, ed. F. Casoli et al. (Les Ulis: EdP-Sciences), 721
- Pound, M. W., & Wolfire, M. G. 2008, in ASP Conf. Ser. 394, Astronomical Data Analysis Software and Systems XVII, ed. R. W. Argyle, P. S. Bunclark, & J. R. Lewis (San Francisco, CA: ASP), 654
- Press, W. H., Teukolsky, S. A., Vetterling, W. T., & Flannery, B. P. 1992, *Numerical Recipes in FORTRAN. The Art of Scientific Computing* (Cambridge: Cambridge Univ. Press)
- Regan, M. W., Thornley, M. D., Helfer, T. T., et al. 2001, *ApJ*, **561**, 218
- Riechers, D. A., Bradford, C. M., Clements, D. L., et al. 2013, *Natur*, **496**, 329
- Riechers, D. A., Capak, P. L., Carilli, C. L., et al. 2010, *ApJL*, **720**, L131
- Riechers, D. A., Carilli, C. L., Capak, P. L., et al. 2014, *ApJ*, **796**, 84
- Roberts-Borsani, G., Morishita, T., Treu, T., Leethochawalit, N., & Trenti, M. 2022, *ApJ*, **927**, 236
- Rosenberg, M. J. F., van der Werf, P. P., Aalto, S., et al. 2015, *ApJ*, **801**, 72
- Rybak, M., da Cunha, E., Groves, B., et al. 2021, *ApJ*, **909**, 130
- Rybak, M., Rivera, G. C., Hodge, J. A., et al. 2019, *ApJ*, **876**, 112
- Saintonge, A., Catinella, B., Tacconi, L. J., et al. 2017, *ApJS*, **233**, 22
- Saintonge, A., Kauffmann, G., Wang, J., et al. 2011, *MNRAS*, **415**, 61
- Saintonge, A., Lutz, D., Genzel, R., et al. 2013, *ApJ*, **778**, 2
- Saintonge, A., Tacconi, L. J., Fabello, S., et al. 2012, *ApJ*, **758**, 73
- Salpeter, E. E. 1955, *ApJ*, **121**, 161
- Sanders, D. B., & Mirabel, I. F. 1996, *ARA&A*, **34**, 749
- Schinnerer, E., Groves, B., Sargent, M. T., et al. 2016, *ApJ*, **833**, 112
- Schmidt, M. 1959, *ApJ*, **129**, 243
- Schouws, S., Stefanon, M., Bouwens, R., et al. 2022, *ApJ*, **928**, 31
- Scoville, N., Sheth, K., Aussel, H., et al. 2016, *ApJ*, **820**, 83
- Sersic, J. L. 1968, *Atlas de Galaxias Australes* (Cordoba: Observatorio Astronomico)
- Shao, Y., Wang, R., Carilli, C. L., et al. 2019, *ApJ*, **876**, 99
- Shibuya, T., Ouchi, M., & Harikane, Y. 2015, *ApJS*, **219**, 15
- Solomon, P. M., & Vanden Bout, P. A. 2005, *ARA&A*, **43**, 677
- Sommovigo, L., Ferrara, A., Carniani, S., et al. 2021, *MNRAS*, **503**, 4878
- Sommovigo, L., Ferrara, A., Pallottini, A., et al. 2020, *MNRAS*, **497**, 956
- Stacey, G. J., Geis, N., Genzel, R., et al. 1991, *ApJ*, **373**, 423
- Stefan, I. I., Carilli, C. L., Wagg, J., et al. 2015, *MNRAS*, **451**, 1713
- Strandet, M. L., Weiss, A., Breuck, C. D., et al. 2017, *ApJL*, **842**, L15
- Sugahara, Y., Inoue, A. K., Hashimoto, T., et al. 2021, *ApJ*, **923**, 5
- Sutter, J., Dale, D. A., Croxall, K. V., et al. 2019, *ApJ*, **886**, 60
- Tacconi, L. J., Genzel, R., & Sternberg, A. 2020, *ARA&A*, **58**, 157
- Tacconi, L. J., Neri, R., Genzel, R., et al. 2013, *ApJ*, **768**, 74
- Tamura, Y., Mawatari, K., Hashimoto, T., et al. 2019, *ApJ*, **874**, 27
- Tody, D. 1986, *Proc. SPIE*, **627**, 733
- Tody, D. 1993, in ASP Conf. Ser. 52, Astronomical Data Analysis Software and Systems II, ed. R. J. Hanisch, R. J. V. Brissenden, & J. Barnes (San Francisco, CA: ASP), 173
- Vallini, L., Ferrara, A., Pallottini, A., Carniani, S., & Gallerani, S. 2021, *MNRAS*, **505**, 5543
- Vallini, L., Ferrara, A., Pallottini, A., & Gallerani, S. 2017, *MNRAS*, **467**, 1300
- Vallini, L., Gallerani, S., Ferrara, A., Pallottini, A., & Yue, B. 2015, *ApJ*, **813**, 36
- Vallini, L., Pallottini, A., Ferrara, A., et al. 2018, *MNRAS*, **473**, 271
- Venemans, B. P., Walter, F., Decarli, R., et al. 2017a, *ApJ*, **845**, 154
- Venemans, B. P., Walter, F., Decarli, R., et al. 2017b, *ApJ*, **837**, 146
- Virtanen, P., Gommers, R., Oliphant, T. E., et al. 2020, *NatMe*, **17**, 261
- Wagg, J., Carilli, C. L., Aravena, M., et al. 2014, *ApJ*, **783**, 71
- Wagg, J., Kanekar, N., & Carilli, C. L. 2009, *ApJL*, **697**, L33
- Wagg, J., Wiklind, T., Carilli, C. L., et al. 2012, *ApJL*, **752**, L30
- Walter, F., Bertoldi, F., Carilli, C., et al. 2003, *Natur*, **424**, 406
- Walter, F., Riechers, D., Novak, M., et al. 2018, *ApJL*, **869**, L22
- Wang, R., Carilli, C. L., Neri, R., et al. 2010, *ApJ*, **714**, 699
- Wang, R., Wagg, J., Carilli, C. L., et al. 2011, *AJ*, **142**, 101
- Wang, R., Wagg, J., Carilli, C. L., et al. 2013, *ApJ*, **773**, 44
- Wang, R., Wu, X.-B., Neri, R., et al. 2016, *ApJ*, **830**, 53
- Weiß, A., De Breuck, C., Marrone, D. P., et al. 2013, *ApJ*, **767**, 88
- Weiß, A., Downes, D., Neri, R., et al. 2007, *A&A*, **467**, 955
- Wright, E. L. 2006, *PASP*, **118**, 1711
- Zanella, A., Daddi, E., Magdis, G., et al. 2018, *MNRAS*, **481**, 1976
- Zavala, J. A., Montaña, A., Hughes, D. H., et al. 2018, *NatAs*, **2**, 56